DQ impedance-decoupled network model-based stability analysis of offshore wind power plant under weak grid conditions

Zhou, Weihua; E. Torres-Olguin, Raymundo; Wang, Yanbo; Chen, Zhe

Published in:
IET Power Electronics

DOI (link to publication from Publisher):
10.1049/iet-pel.2019.1575

Publication date:
2020

Document Version
Accepted author manuscript, peer reviewed version

IET Power Electronics

Special Issue: Harmonic Mitigation Techniques and Grid Robustness in Power Electronic-Based Power Systems

IET Journals
The Institution of Engineering and Technology

ISSN 1751-8644
doi: 0000000000
www.ietdl.org

DQ impedance-decoupled network model-based stability analysis of offshore wind power plant under weak grid conditions

Weihua Zhou[1], *Raymundo E. Torres-Olguin*[2], *Yanbo Wang*[1] ✉, *Zhe Chen*[1]

[1] *Department of Energy Technology, Aalborg University, Aalborg 9220, Denmark*
[2] *SINTEF Energy Research Institute, Trondheim 7034, Norway*
✉ *E-mail: ywa@et.aau.dk*

Abstract: Instability phenomena of an offshore wind power plant (OWPP) may occur in a wide frequency range, due to impedance interactions between control loops of grid-connected inverters (GCIs) and long transmission cable (LTC) networks. This paper presents a dq impedance-decoupled network modelling method of OWPP for stability analysis. DQ impedance frequency responses of GCIs and LTCs are first measured by frequency scanning method, which are fitted as transfer function matrices based on matrix fitting algorithm. Then, the GCIs are modelled as Norton equivalent circuits. In addition, per-unit-length electrical parameters, e.g., resistance, inductance and capacitance, of the LTCs are extracted from the measured dq impedance frequency responses of a specific LTC, based on which dq impedance-decoupled two-port network models of the LTCs are established. DQ impedance-decoupled network model of the whole OWPP is then established based on connection relationships of these GCIs and LTCs. Finally, generalized Nyquist criterion (GNC) is performed in all the dq impedance-decoupled subsystems, and the subsystems where the GNC is not satisfied are identified as instability sources. Compared with conventional impedance-based stability analysis methods of OWPP, the proposed dq impedance-decoupled modelling method is able to facilitate the application of GNC and further instability source identification based on partitioning the whole OWPP into several decoupled subsystems. The effectiveness of the dq impedance-decoupled network modelling method for stability analysis is validated in a typical type-IV permanent magnet synchronous generator-based OWPP under weak grid conditions based on time-domain simulation results in Matlab/Simulink platform and real-time verification results in OPAL-RT platform.

1 Introduction

Offshore wind power plants (OWPPs) have been gaining increasing concerns, due to abundant wind power resources, little visual and auditory noise, and no occupied spaces [1]. Voltage source grid-connected inverters (GCIs), as important interfaces, are commonly used to transfer the generated electrical energy to utility grid [2]. Impedance interactions between control loops of the GCIs and long transmission cables (LTCs) could result in instability phenomena in a wide frequency range, which threaten safe and reliable operation of the whole system [3–6]. Specifically, low-frequency instability phenomena may be caused due to improper designs of phase-locked loop (PLL) and outer control loops, e.g., dc-link voltage control loop and power control loop [7–11]. In addition, improper design of inner current control loop may lead to high-frequency instability phenomena under weak grid conditions [12–14]. For simplicity, only PLL and inner current control loop, as representatives, will be investigated in this paper. It's necessary to establish an efficient system model and develop corresponding stability criteria to identify the instability phenomena and corresponding problematic components at the initial design stage.

The small-signal stability of power electronic-dominated AC power systems has conventionally been investigated by system state-space model [7, 15–17]. However, heavy computational burdens are involved in power systems with moderate to large size. In addition, the detailed information of control structure and parameters are required. Recently, the impedance-based stability criterion (IBSC), as an alternative method, has widely been applied, where the overall system is partitioned into source and load parts at a certain bus, and both right-half plane (RHP) poles of the impedance ratio and the encirclement number of the Nyquist plot of the impedance ratio around $(-1, j0)$ in the complex plane are calculated [18, 19]. The main step of the IBSC is to establish the component impedance model. Specifically, dq impedance model has widely been used to assess stability related to the inner current control loop and PLL [20–22]. It is revealed in [20, 22] that the negative-resistor behaviour of PLL in low-frequency range could result in instability phenomena under weak grid conditions, which can be captured by q-q channel component of the dq impedance model. Since both source and load parts of single GCI-based system are inherently stable, no RHP poles calculation is needed [18, 20, 22]. However, when the conventional IBSC is applied in an OWPP where a large number of GCIs and LTCs exist, RHP poles calculation cannot be avoided. In addition, problematic components cannot be identified, since the GCIs and LTCs are aggregated for IBSC. The dq impedance formulas of source and load parts, thus, should be theoretically derived to calculate the RHP poles. However, the theoretically-derived dq impedance models of source and load parts may have very high orders, due to the existence of a large number of GCIs and LTCs. In addition, the dq impedance models sometimes cannot be theoretically derived, due to industry confidentiality about internal structure and parameters of the GCIs.

Many works have been reported to avoid RHP poles calculation for stability assessment of large-scale power electronic-based AC power systems [4, 23–34]. In [23], the theoretically-derived dq impedance models of the GCIs and transmission lines are connected based on system topology, based on which a loop impedance model is derived. The determinant of the loop impedance model is then calculated to assess system stability. Different from [23], dq impedance formulas of the GCIs are fitted from measured impedance frequency responses based on system identification technique in [24, 25]. RHP poles calculation can be avoided. Instability sources, however, cannot be identified, since information of system structure is missing in the loop impedance model [23–26]. Similarly,

the impedance frequency responses of the whole power systems at a specific node are fitted as a state-space model using the vector fitting (VF) or matrix fitting (MF) algorithm in [27, 35]. In addition, the terminal impedance frequency responses of the subsystems and individual components are fitted as state-space models using the VF or MF algorithm in [28] and [29], respectively. RHP poles calculation can also be avoided in [27–29]. However, the stability analysis methods presented in [27–29] are system state space-based eigenvalues analysis instead of impedance-based stability analysis. In [4, 30, 31], information about system structure is maintained by the nodal admittance matrix. System stability can then be assessed by the determinant of the nodal admittance matrix, and contributions of all components on system modes of interest can be calculated by participation factor analysis. However, when there exists a huge number of nodes, the order of the nodal admittance matrix is very high, and heavy computational burdens will be involved.

On the other hand, the Nyquist stability criterion is performed sequentially from the farthest bus to point of common coupling (PCC) in [23, 32–34], where RHP poles calculation is avoided. In each step, ratio of the nearest component impedance which is at the right side of a bus and total impedance which is at the left side of the bus is calculated, based on which the encirclement number around $(-1, j0)$ of Nyquist plot of the impedance ratio is counted. If the encirclement number is not zero at a certain bus, the overall system is assessed as unstable. It can be seen that RHP poles calculation can be avoided, and instability sources can be identified. However, the multi-step Nyquist stability criterion-based stability analysis method needs to calculate the aggregated impedance models at all buses sequentially, which tends to bring in heavy computational burdens. In addition, only purely inductive transmission lines are considered in [23, 32–34], where practical parasitic capacitances along the LTCs is not taken into account. The LTCs may complicate the stability analysis procedure based on the multi-step Nyquist stability criterion. Impedance-decoupled two-port network model of the LTC with consideration of parasitic capacitance is proposed in [5, 36] to facilitate stability analysis. However, only single GCI is investigated in [36], and multiple GCIs connected with PCC are investigated in [5]. The practical radial topology of the OWPP is not considered in [5, 36]. Furthermore, impedance-decoupled multi-port network models of multi-port transmission networks are presented in [13, 33]. However, the presented modelling methods in [13, 33] are not applicable for LTC, since the parasitic capacitance is also not considered. In addition, the impedance-decoupled two-port or multi-port network model is established in phasor-domain, which is not suitable for PLL-related low-frequency stability analysis, i.e., the LTC model should be established in dq-domain.

The per-unit-length (p.u.l.) electrical parameters of the LTCs, e.g., p.u.l. resistance and p.u.l. inductance, are commonly assumed as not frequency dependent in previous works [3, 37, 38]. In practice, the p.u.l. inductance decreases as frequency increases, whereas the p.u.l. resistance increases as frequency increases [39]. Therefore, this simplification may lead to inaccurate stability analysis results, since the inherent damping characteristics of the LTCs in high-frequency range are ignored [10, 40, 41]. The frequency-dependent characteristics will, thus, be considered in this paper for accurate stability analysis results . However, the measurement of terminal impedance frequency responses of the LTCs can be tedious and time-consuming, if many LTCs exist in the OWPP. In [42, 43], the frequency-dependent p.u.l. electrical parameters of the power cables are extracted from measured terminal impedance frequency responses of a specific power cable, and used to calculate the terminal impedance formulas of the same type of power cables in other lengths. However, the studied power cables in [42, 43] are commonly in length of tens of metres, which is not suitable for the LTC which can be tens or hundreds of kilometres.

This paper further develops the multi-step Nyquist stability criterion presented in [23, 32–34] by splitting the whole OWPP into several decoupled subsystems with the help of the dq impedance-decoupled two-port network model of the LTC. The overall system is first partitioned into individual components, e.g., GCIs and LTCs. The dq impedance frequency responses of all GCIs are then measured by performing frequency scanning, which are fitted as transfer function matrices using the MF algorithm. In addition, all LTCs are divided into different categories according to materials and geometrical shapes, so that each kind of LTC has the same p.u.l. electrical parameters. For each kind of LTC, one-end short-circuited and one-end open-circuited terminal impedance frequency responses are obtained by performing frequency scanning, based on which the p.u.l. electrical parameters are then identified. Then, the dq impedance models of the LTCs in other lengths can be theoretically calculated. The GCIs and LTCs can then be modelled as Norton equivalent circuits and dq impedance-decoupled two-port circuit models, respectively. Based on their interconnection relationship, the established component circuit models are integrated, and the impedances of adjacent GCIs and LTCs are aggregated based on one-end open-circuited admittances of LTCs. Generalized Nyquist criterion (GNC) is applied in all the decoupled subsystems, and the subsystems which do not satisfy GNC are identified as instability sources.

The main contributions of this paper are explained as follows.

1) A frequency-dependent p.u.l. electrical parameters identification method of the LTC is proposed, which is able to facilitate impedance modelling of LTCs of the same material but in different lengths.

2) A unified dq impedance model fitting method of GCIs and LTCs based on the MF algorithm is proposed, which is able to deal with variation and uncertainty of internal structure and parameters.

3) An admittance aggregation method of GCI and LTC based on one-end open-circuited admittance of LTC is proposed, where no information about series impedance and shunt admittance of the LTC is required.

4) A dq impedance-decoupled network modelling method of OWPP is proposed, which partitions the whole OWPP into several decoupled subsystems. It's able to facilitate stability analysis and problematic components identification based on the multi-step Nyquist stability criterion.

The rest of this paper is organized as follows. Theory basis is introduced in Section 2. In Section 3, principle of the dq impedance-decoupled network modelling method and detailed implementation procedure are explained. In addition, some issues about the proposed stability analysis method are also discussed. The proposed stability analysis method is performed in a typical OWPP in Section 4. Section 5 verifies the correctness of the stability analysis results in Section 4 based on time-domain simulation results in Matlab/Simulink platform and real-time verification results in OPAL-RT platform. Finally, conclusions are drawn in Section 6.

2 Theory Basis

In this section, theory basis of the proposed dq impedance-decoupled network modelling method of OWPPs is introduced. In detail, dq impedance frequency characteristics of both GCIs and LTCs are fist reviewed, followed by introduction of the MF algorithm.

2.1 DQ Impedance Model of the GCIs

Fig. 1 shows the configuration of a typical HVAC permanent magnet synchronous generator (PMSG)-based OWPP. Control of the rectifier and the GCI in the PMSG system is decoupled, and dc-link voltage can be regarded as constant [3]. Fig. 2 shows the control diagram of an L-filtered GCI, where current control loop and PLL are used to track current reference i^*_{tdq} and phase angle of terminal voltage v_{tabc}, respectively. Due to asymmetric impact of PLL on terminal impedance, 2×2 impedance matrix in dq domain shown as (1) should be used [20].

$$\mathbf{Z_{dq\_L}} = (\mathbf{Y^c_L} - V_{dc}\mathbf{Y^g_L}\mathbf{G_{del}}(-\mathbf{G_{ci}}\mathbf{G^i_{PLL}} + \mathbf{G^d_{PLL}}))^{-1} \cdot(\mathbf{I} + V_{dc}\mathbf{Y^g_L}\mathbf{G_{del}}\mathbf{G_{ci}}) \quad (1)$$

where bold letters indicate 2×2 matrices. $\mathbf{G^i_{PLL}}$ and $\mathbf{G^d_{PLL}}$ are two asymmetric matrices related with PLL. Expressions of transfer function matrices in (1) can be found in the Appendix.

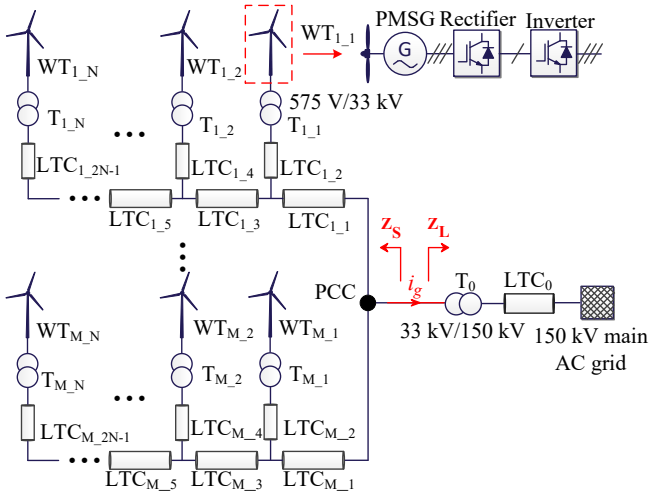

Fig. 1. Configuration of a typical HVAC PMSG-based OWPP.

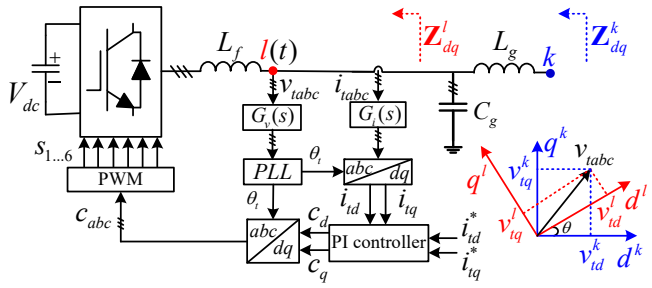

Fig. 2. Control diagram of an L-filtered GCI with current control loop and PLL.

In addition, the dq impedance matrix of an LCL-filtered GCI can be obtained based on (1), shown as

$$\begin{aligned}\mathbf{Z_{dq\_LCL}} = (\mathbf{Y^c_{LCL}} - V_{dc}\mathbf{Y^g_{LCL}}\mathbf{G_{del}}(-\mathbf{G_{ci}}\mathbf{G^i_{PLL}} + \mathbf{G^d_{PLL}}))^{-1} \\ \cdot(\mathbf{I} + V_{dc}\mathbf{Y^g_{LCL}}\mathbf{G_{del}}\mathbf{G_{ci}})\end{aligned} \tag{2}$$

where detailed expression of each symbol is also shown in the Appendix.

The dq impedance matrices $\mathbf{Z_{dq\_L}}$ and $\mathbf{Z_{dq\_LCL}}$ are aligned to terminal voltage v_{tabc}. Therefore, $\mathbf{Z_{dq\_L}}$ and $\mathbf{Z_{dq\_LCL}}$ in l and k reference frames are not the same, which can be linked by (3) [23].

$$\begin{aligned}\mathbf{Z^k_{dq\_L}} &= \mathbf{R_{dq}}(\theta)\mathbf{Z^l_{dq\_L}}\mathbf{R^{-1}_{dq}}(\theta) \\ \mathbf{Z^k_{dq\_LCL}} &= \mathbf{R_{dq}}(\theta)\mathbf{Z^l_{dq\_LCL}}\mathbf{R^{-1}_{dq}}(\theta)\end{aligned} \tag{3}$$

where $\mathbf{R}_{dq}(\theta) = [\cos\theta, \sin\theta; -\sin\theta, \cos\theta]$ is rotation matrix, and θ is the difference of voltage angles at nodes l and k.

Besides PLL and inner current control loop shown in Fig. 2, the effects of outer dc-link voltage control loop and outer power control loop on dq impedance model of the GCI have been investigated in [9] and [8, 10], respectively. The studies show that, similar with PLL, outer dc-link voltage control loop and outer power control loop also affect the dq impedance characteristics of the GCI in low-frequency range, thus affecting system low-frequency stability, since the bandwidths of PLL, outer dc-link voltage control loop and outer power control loop are designed to be close to each other and much lower than the bandwidth of inner current control loop [44, 45].

This paper aims to present a dq impedance-decoupled network modelling method to facilitate the identification of the instability phenomena in both high-frequency and low-frequency ranges, instead of investigating the effects of various control loops on system

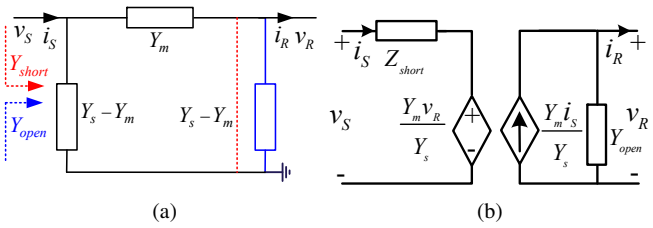

Fig. 3. Circuit model of an LTC. (a) Single-Π model with lumped parameters. (b) Impedance-decoupled two-port circuit model.

stability. Therefore, the current control loop-related high-frequency stability issue and PLL-related low-frequency stability issue, as representatives, are used to verify the validity of the proposed method in this paper. The dc-link voltage dynamics are, thus, neglected by assuming a large dc-link capacitor. In fact, similar simplification has been widely adopted in existing works. For example, the dynamics of dc-link voltage control and PLL are neglected in [3, 4, 46, 47] where high-frequency harmonic instability is focused. In addition, the dc-link voltage is assumed as constant in [8, 48] to focus on the PLL-related low-frequency stability issue. Readers can find detailed impedance modelling procedure of the PMSG in [49, 50], where dc-link voltage dynamics are considered.

2.2 *Terminal Impedance Characteristics of the LTCs*

Voltage and current distribution along a uniform LTC can be expressed as following classical telegraph equations [36, 51].

$$\begin{aligned}\partial_x v(x,\omega) &= -Z'(\omega)i(x,\omega) \\ \partial_x i(x,\omega) &= -Y'(\omega)v(x,\omega)\end{aligned} \tag{4}$$

where $v(x,\omega)$ and $i(x,\omega)$ are voltage and current at position x of the LTC, respectively. $Z'(\omega) = R'(\omega) + j\omega L'(\omega)$ and $Y'(\omega) = G'(\omega) + j\omega C'(\omega)$ are p.u.l. series impedance and shunt admittance of the LTC, respectively. In general, $G'(\omega)$ can be ignored and $C'(\omega)$ can be regarded as constant [51]. In addition, $L'(\omega)$ decreases as frequency ω increases, whereas $R'(\omega)$ increases as frequency ω increases [39, 41]. If the frequency-dependent characteristics of $L'(\omega)$ and $R'(\omega)$ are ignored, inaccurate stability analysis conclusions may be obtained [10, 40].

(4) can be rewritten as a 2-order differential equation to decouple $v(x,\omega)$ and $i(x,\omega)$, shown as

$$\begin{aligned}\partial^2_x v(x,\omega) &= Z'(\omega)Y'(\omega)v(x,\omega) = \gamma^2(\omega)v(x,\omega) \\ \partial^2_x i(x,\omega) &= Z'(\omega)Y'(\omega)i(x,\omega) = \gamma^2(\omega)i(x,\omega)\end{aligned} \tag{5}$$

where $\gamma(\omega) = \sqrt{(Z'(\omega)Y'(\omega))}$ is the propagation constant.

Based on (5), the currents flowing through both ends can be expressed by the voltages at both ends, shown as

$$\begin{bmatrix} i_S \\ -i_R \end{bmatrix} = \begin{bmatrix} Y_s & -Y_m \\ -Y_m & Y_s \end{bmatrix} \begin{bmatrix} v_S \\ v_R \end{bmatrix} \tag{6}$$

where Y_s and Y_m represent self admittance and mutual admittance, respectively, which are expressed as

$$\begin{aligned}Y_s &= 1/(Z_c \tanh(\gamma\ell)) \\ Y_m &= 1/(Z_c \sinh(\gamma\ell))\end{aligned} \tag{7}$$

where ω is omitted for simplicity, and $Z_c = \sqrt{Z'/Y'}$ is the characteristic impedance.

Based on (6), the LTC can be modelled as a lumped-parameter single-Π model, as shown in Fig. 3(a). In addition, the equivalent two-port circuit model is established in Fig. 3(b), where Z_{short}

and Y_{open} are one-end short-circuited impedance and one-end open-circuited admittance, respectively, shown as

$$Z_{short} = Y_{short}^{-1} = Y_s^{-1}$$
$$Y_{open} = Z_{open}^{-1} = (Y_s^2 - Y_m^2)/Y_s \quad (8)$$

Then, one-end short-circuited dq impedance and one-end open-circuited dq admittance can be calculated based on (8), shown as [48]

$$\mathbf{Z_{short}^{dq}} = \mathbf{A_Z^{-1}} \mathbf{Z_{short}^{pn}} \mathbf{A_Z} = \mathbf{A_Z^{-1}} \begin{bmatrix} Z_{short}^{pp} & Z_{short}^{pn} \\ Z_{short}^{np} & Z_{short}^{nn} \end{bmatrix} \mathbf{A_Z}$$
$$\mathbf{Y_{open}^{dq}} = \mathbf{A_Z^{-1}} \mathbf{Y_{open}^{pn}} \mathbf{A_Z} = \mathbf{A_Z^{-1}} \begin{bmatrix} Y_{open}^{pp} & Y_{open}^{pn} \\ Y_{open}^{np} & Y_{open}^{nn} \end{bmatrix} \mathbf{A_Z} \quad (9)$$

where $\mathbf{A_Z} = \frac{1}{\sqrt{2}}[1, j; 1, -j]$ and $Z_{short}^{pn} = Z_{short}^{np} = Y_{open}^{pn} = Y_{open}^{np} = 0$. In addition,

$$Z_{short}^{pp} = Z_{short}(s + j\omega_1)$$
$$Z_{short}^{nn} = Z_{short}(s - j\omega_1)$$
$$Y_{open}^{pp} = Y_{open}(s + j\omega_1)$$
$$Y_{open}^{nn} = Y_{open}(s - j\omega_1) \quad (10)$$

where ω_1 is the fundamental angular frequency.

The motivation why the single-Π model with lumped parameters in Fig. 3(a) is represented as the two-port circuit model in Fig. 3(b) based on one-end short-circuited impedance Z_{short} and one-end open-circuited admittance Y_{open} can be explained as follows. First, the two-port circuit model in Fig. 3(b) is able to facilitate the proposed p.u.l. electrical parameters identification method shown in Section 3.3, since the identification method is based on measured terminal impedance frequency responses, i.e., Z_{short} and Y_{open}. Second, the two-port circuit model in Fig. 3(b) contributes to establishing the dq impedance-decoupled network model of the whole OWPP, as shown in Section 3.4.

2.3 MF Algorithm

A series of discrete frequency responses of a multiple-input multiple-output (MIMO) system can be fitted as a rational model in pole-residue form by the MF algorithm [35]. Taking a k-port MIMO system as an example, the fitted transfer function matrix is given as [35]

$$\mathbf{F(s)} = \frac{\mathbf{R}_m}{s - p_m} + \frac{\mathbf{R}_{m-1}}{s - p_{m-1}} ... + \frac{\mathbf{R}_1}{s - p_1} + \mathbf{D} + s\mathbf{E}$$
$$= \mathbf{C}(s\mathbf{I} - \mathbf{A})^{-1}\mathbf{B} + \mathbf{D} + s\mathbf{E} \quad (11)$$

where $\mathbf{A} = diag(diag(p_1, p_2...p_m), ..., diag(p_1, p_2...p_m))_k$, $\mathbf{B} = diag([1, 1, ...1]_m{}^T, ..., diag[1, 1, ...1]_m{}^T)_k$, $\mathbf{C} = [\mathbf{R}_1(:, 1), \mathbf{R}_2(:, 1)$ $..., \mathbf{R}_m(:, 1), \mathbf{R}_1(:, 2), \mathbf{R}_2(:, 2)..., \mathbf{R}_m(:, 2), ..., \mathbf{R}_1(:, k), \mathbf{R}_2(:, k)$ $..., \mathbf{R}_m(:, k)]$. Both $\mathbf{D}$ and $\mathbf{E}$ are $k \times k$ matrices. It can be seen from (11) that all elements in $\mathbf{F}(s)$ share the same poles sets $(p_1, p_2..., p_m)$, which can be used to assess stability issue of the MIMO system.

3 Proposed Stability Analysis Method Based on DQ Impedance-Decoupled Network Model

In this section, the implementation procedure of the proposed stability analysis method based on dq impedance-decoupled network model is first introduced. On the basis of it, each step is explained in detail. Finally, some issues related to the proposed stability analysis method are discussed.

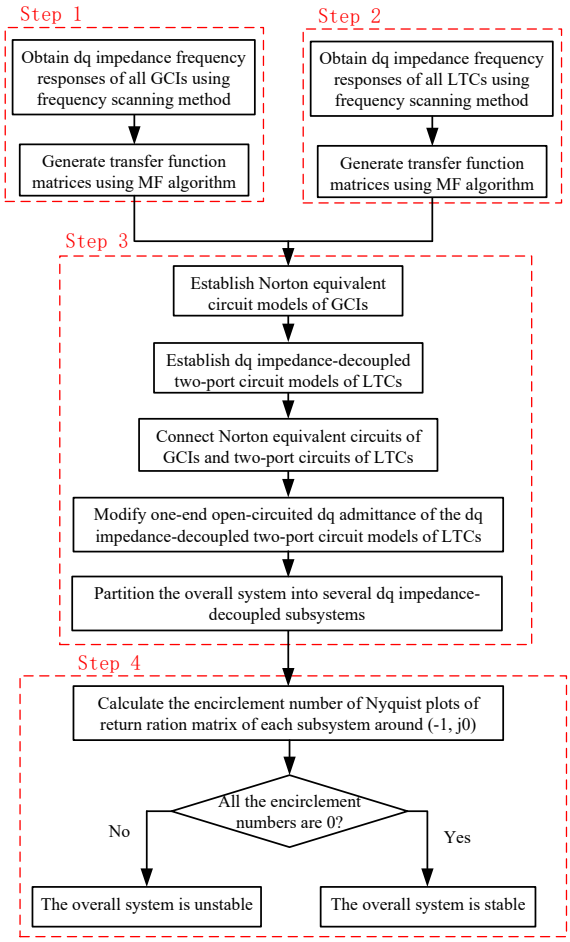

Fig. 4. Flowchart of the proposed dq impedance-decoupled network modelling method for stability analysis.

3.1 Flowchart of the Proposed Stability Analysis Method

Fig. 4 shows the flowchart of the proposed dq impedance-decoupled network modelling method for stability analysis. In step 1, impedance frequency responses of all GCIs in dq-domain are measured using the frequency scanning method. On the basis of it, the transfer function matrices are fitted using the MF algorithm. In step 2, terminal impedance frequency responses of an LTC are measured in phasor-domain, from which the p.u.l. parameters are extracted. Then, dq impedance models of all LTCs in different lengths can be calculated. In step 3, Norton equivalent circuits of GCIs and dq impedance-decoupled two-port circuit models of LCTs are established and connected based on their connection relationship. In addition, the dq impedance models of adjacent GCIs and LTCs are aggregated, and the overall system is partitioned into several subsystems. In step 4, GNC is performed in all dq impedance-decoupled subsystems. If encirclement numbers of Nyquist plots of characteristics loci of return ratio matrices of all subsystems around $(-1, j0)$ are zero, the OWPP is assessed as stable. Otherwise, the OWPP is probably unstable.

3.2 Step 1: Identification of DQ Impedance Models of GCIs from Measured Terminal Impedance Frequency Responses

Identification of dq impedance models of the GCIs consists of two main steps.

3.2.1 Measurement of DQ Impedance Frequency Responses:

The frequency scanning method is depicted in Fig. 5, where a small-signal voltage perturbation v_{inj} is injected into PCC in series way

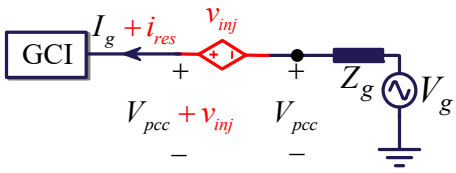

Fig. 5. Measurement of dq impedance frequency responses of the GCI using frequency scanning method.

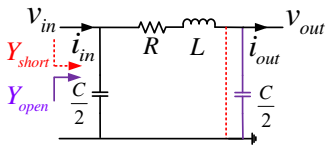

Fig. 6. Simplified single-Π circuit model of the LTC without considering frequency-dependent characteristic.

to excite the small-signal current response i_{res} (A small-signal current perturbation i_{inj} can also be injected into PCC in parallel way to excite the small-signal voltage response v_{res}). Magnitude of v_{inj} cannot be too large, so that the operation point of the GCI can be kept almost unchanged [52]. The excitation signal v_{inj} consists of multiple frequency components which are commonly evenly distributed or logarithmically distributed in the frequency range of interest. In addition, two sets of linear independent perturbation signals v_{inj} are applied separately in dq domain, since the dq impedance model is represented as a 2×2 matrix. FFT is then performed to analyse v_{inj} and i_{res}, and Park transformation is applied to obtain equivalent representations in dq frame, i.e., v_{injdq} and i_{resdq}, at all frequency points. The measured dq impedance frequency responses $\mathbf{Z_{dq\_mea}}$ can be calculated as

$$\mathbf{Z_{dq\_mea}} = \begin{bmatrix} v_{injd} \\ v_{injq} \end{bmatrix} \begin{bmatrix} i_{resd} \\ i_{resq} \end{bmatrix}^{-1} \tag{12}$$

3.2.2 Generate Transfer Function Matrix from Measured DQ Impedance Frequency Responses: Transfer function matrix in the form of (11) is generated from the measured impedance frequency responses in (12) using the MF algorithm, where the order m is determined in a trial-and-error way. In detail, m is gradually increased until the fitting error is acceptable.

3.3 Step 2: Identification of DQ impedance Models of Length-Scalable LTCs from Measured Terminal Impedance Frequency Responses

By substituting (7) into (8), γ and Z_c can be calculated from Y_{short} and Y_{open}, shown as

$$\begin{aligned} \gamma &= \left(\cosh^{-1} \left(\sqrt{\frac{Y_{short}}{Y_{short} - Y_{open}}} \right) + j2\pi k \right) / \ell \quad k \in Z \\ Z_c &= \frac{1}{\sqrt{Y_{open} Y_{short}}} \end{aligned} \tag{13}$$

Then, p.u.l. series impedance Z' and shunt admittance Y' can be derived as

$$\begin{aligned} Z' &= R' + j\omega L' = \gamma Z_c = \frac{\gamma}{\sqrt{Y_{open} Y_{short}}} \\ Y' &= j\omega C' = \gamma / Z_c = \gamma \sqrt{Y_{open} Y_{short}} \end{aligned} \tag{14}$$

where $R' = Re(\gamma Z_c)$, $L' = Im(\gamma Z_c)/\omega$ and $C' = Im(\gamma / Z_c)/\omega$.

Based on the identified R', L' and C', the two-port circuit models of the LTCs in other lengths can be established based on (7) and (8). Impedance/admittance model in dq domain can further be calculated based on (9) and (10).

Here gives the theoretical verification of the effectiveness of the proposed p.u.l. electrical parameters extraction method. Assume that an LTC with length d_0, p.u.l. resistance R', inductance L' and capacitance C' is studied (The frequency-dependent characteristics of p.u.l. parameters are ignored to simplify the verification process. However, the conclusion is also applicable when frequency-dependent characteristic is considered, as shown in Section 4.2). Single-Π RLC circuit model in form of Fig. 3(a) can be obtained, as shown in Fig. 6. One-end open-circuited and short-circuited admittances seen from the sending end of the LTC are as

$$\begin{aligned} Y_{short} &= \frac{1}{sL + R} + \frac{sC}{2} \\ Y_{open} &= \frac{1}{\frac{2}{sC} + sL + R} + \frac{sC}{2} \end{aligned} \tag{15}$$

where $R = R'd_0$, $L = L'd_0$ and $C = C'd_0$.

The propagation constant can be calculated by (13), shown as

$$\begin{aligned} \gamma_{cal} &= \left(\cosh^{-1} \left(\frac{d_0^2 (s^2 L'C' + sR'C')}{2} + 1 \right) + j2\pi k \right) / d_0 \\ &= \left(\cosh^{-1} \left(\frac{d_0^2 \gamma_{theo}^2}{2} + 1 \right) + j2\pi k \right) / d_0 \quad k \in Z \end{aligned} \tag{16}$$

where $\gamma_{theo} = \sqrt{(sL' + R')sC'}$ is the theoretical propagation constant. (16) provides the relationship between the derived propagation constant using terminal admittances γ_{cal} and the theoretical propagation constant γ_{theo}.

To quantify the calculation error, Taylor series expansion of the hyperbolic cosine function $cosh(\gamma_{theo} d_0)$ is shown as

$$\begin{aligned} \cosh(\gamma_{theo} d_0) = \frac{e^{\gamma_{theo} d_0} + e^{-\gamma_{theo} d_0}}{2} &= 1 + \frac{(\gamma_{theo} d_0)^2}{2!} \\ + \frac{(\gamma_{theo} d_0)^4}{4!} + \frac{(\gamma_{theo} d_0)^6}{6!} &\ldots \end{aligned} \tag{17}$$

In principle, infinite cascaded Π sections can accurately reproduce terminal impedance characteristics of the LTC, which means that the LTC length represented by each Π section approximates to 0. Thus, the high-order terms in (17) can be omitted, and the following equation can be obtained.

$$\gamma_{theo} d_0 \approx \cosh^{-1}(1 + \frac{(\gamma_{theo} d_0)^2}{2!}) + j2\pi k \quad k \in Z \tag{18}$$

By substituting (18) into (16), it can be found that,

$$\gamma_{cal} \approx \gamma_{theo} = \sqrt{(sL' + R')sC'} \tag{19}$$

It shows that the proposed method can accurately extract the propagation constant γ_{theo} from Y_{short} and Y_{open}.

3.4 Step 3: Establishment of the DQ Impedance-Decoupled Network Model of the Whole OWPP

Based on the fitted dq impedance models of GCIs and LTCs, the corresponding Norton equivalent circuits of GCIs and dq impedance-decoupled two-port circuit models of LTCs as shown in Fig. 3(b) are established. Then, the circuit models of GCIs and LTCs are connected together based on their connection relationship. For example, Fig. 7(a) shows a simplified radial OWPP with three GCIs and five LTCs. Its equivalent circuit model can be established as Fig. 7(b).

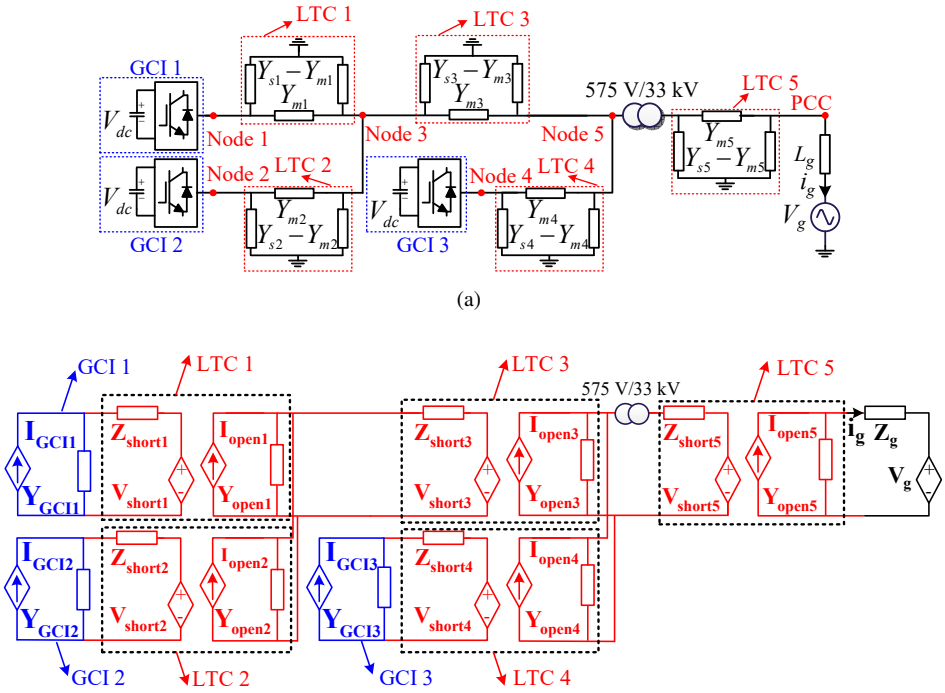

Fig. 7. Implementation of the proposed dq impedance-decoupled network model for stability analysis. (a) Circuit model of a three-GCI-based radial OWPP. (b) Established equivalent circuit model.

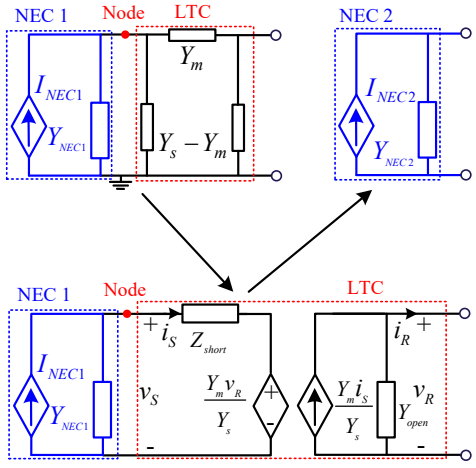

Fig. 8. Aggregation of a Norton equivalent circuit and an LTC.

Next, the circuit models of adjacent GCIs and LTCs in Fig. 7(b) are aggregated sequentially from node 1 to node 5, which follows the aggregation principle shown in Fig. 8 [53]. In detail, a Norton equivalent circuit NEC 1 and an LTC can be aggregated as a Norton equivalent circuit NEC 2, where the parameters are

$$\begin{aligned} I_{NEC2} &= \frac{Y_m I_{NEC1}}{Y_{NEC1} + (Y_s - Y_m) + Y_m} = \frac{Y_s^{-1} Y_m I_{NEC1}}{1 + Y_s^{-1} Y_{NEC1}} \\ Y_{NEC2} &= \frac{1}{\frac{1}{Y_{NEC1} + Y_s - Y_m} + \frac{1}{Y_m}} + Y_s - Y_m \\ &= \frac{Y_{NEC1} + Y_s - Y_s^{-1} Y_m^2}{1 + Y_s^{-1} Y_{NEC1}} \end{aligned} \tag{20}$$

By substituting (8) into (20), the parameters of NEC 2 can be reformulated as

$$\begin{aligned} I_{NEC2} &= \frac{\sqrt{1 - Y_{open} Z_{short}}\, I_{NEC1}}{1 + Z_{short} Y_{NEC1}} \\ Y_{NEC2} &= \frac{(1 + Z_{open} Y_{NEC1}) Y_{open}}{(1 + Z_{short} Y_{NEC1})} \end{aligned} \tag{21}$$

Similar with (21), GCI 1 and LTC 1 can be aggregated at node 1 into a Norton equivalent circuit, of which the current source and equivalent admittance can be calculated as

$$\begin{aligned} I_{N1} &= \frac{\sqrt{1 - Y_{open1} Z_{short1}}}{1 + Z_{short1} Y_{GCI1}} I_{GCI1} \\ Y_{N1} &= \frac{1 + Z_{open1} Y_{GCI1}}{1 + Z_{short1} Y_{GCI1}} Y_{open1} \end{aligned} \tag{22}$$

To depict the aggregation effect, I_{open1} and Y_{open1} are modified as I_{N1} and Y_{N1}, respectively. In addition, GCI 2 and LTC 2 can be aggregated at node 2 into a Norton equivalent circuit, of which the current source and equivalent admittance can be calculated as

$$\begin{aligned} I_{N2} &= \frac{\sqrt{1 - Y_{open2} Z_{short2}}}{1 + Z_{short2} Y_{GCI2}} I_{GCI2} \\ Y_{N2} &= \frac{1 + Z_{open2} Y_{GCI2}}{1 + Z_{short2} Y_{GCI2}} Y_{open2} \end{aligned} \tag{23}$$

Similarly, I_{open2} and Y_{open2} are modified as I_{N2} and Y_{N2}, respectively. Furthermore, the two modified Norton equivalent circuits established in (22) and (23) can be aggregated with LTC 3 at node 3 into a Norton equivalent circuit, of which the current source

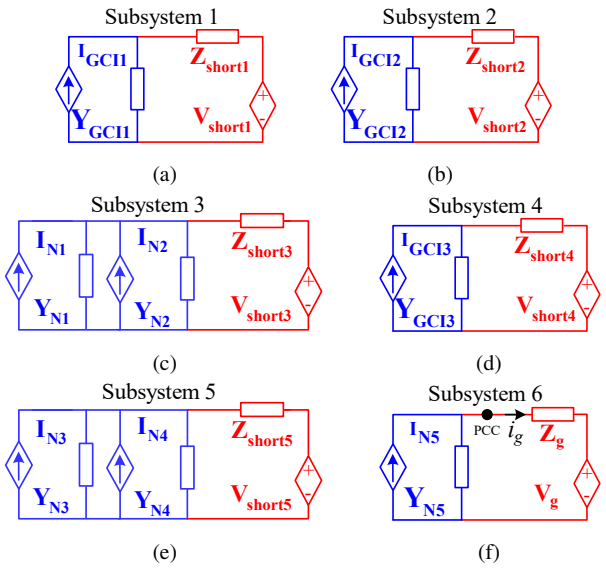

Fig. 9. Six modified subsystems of Fig. 7(b). (a) Subsystem 1. (b) Subsystem 2. (c) Subsystem 3. (d) Subsystem 4. (e) Subsystem 5. (f) Subsystem 6.

and equivalent admittance can be calculated as

$$I_{N3} = \frac{\sqrt{1 - Y_{open3}Z_{short3}}}{1 + Z_{short3}(Y_{N1} + Y_{N2})}(I_{N1} + I_{N2})$$
$$Y_{N3} = \frac{1 + Z_{open3}(Y_{N1} + Y_{N2})}{1 + Z_{short3}(Y_{N1} + Y_{N2})}Y_{open3} \quad (24)$$

I_{open3} and Y_{open3} are modified as I_{N3} and Y_{N3}, respectively. Similarly with (22) and (23), GCI 3 and LTC 4 can be aggregated at node 4 into a Norton equivalent circuit, of which the current source and equivalent admittance can be calculated as

$$I_{N4} = \frac{\sqrt{1 - Y_{open4}Z_{short4}}}{1 + Z_{short4}Y_{GCI3}}I_{GCI3}$$
$$Y_{N4} = \frac{1 + Z_{open4}Y_{GCI3}}{1 + Z_{short4}Y_{GCI3}}Y_{open4} \quad (25)$$

I_{open4} and Y_{open4} are modified as I_{N4} and Y_{N4}, respectively. Similarly with (24), the two modified Norton equivalent circuits established in (24) and (25) can be aggregated with LTC 5 at node 5 into a Norton equivalent circuit, of which the current source and equivalent admittance can be calculated as

$$I_{N5} = \frac{\sqrt{1 - Y_{open5}Z_{short5}}}{1 + Z_{short5}(\frac{Y_{N3}}{K_T^2} + \frac{Y_{N4}}{K_T^2})}(\frac{I_{N3}}{K_T} + \frac{I_{N4}}{K_T})$$
$$Y_{N5} = \frac{1 + Z_{open5}(\frac{Y_{N3}}{K_T^2} + \frac{Y_{N4}}{K_T^2})}{1 + Z_{short5}(\frac{Y_{N3}}{K_T^2} + \frac{Y_{N4}}{K_T^2})}Y_{open5} \quad (26)$$

where $K_T = \frac{33000}{575} = 57.39$ is the set-up ratio of the ideal transformer in Fig. 7(a). I_{open5} and Y_{open5} are modified as I_{N5} and Y_{N5}, respectively.

Based on the components aggregation procedure in (22)-(26), the whole OWPP in Fig. 7(b) can be divided into six subsystems, as shown in Fig. 9. Then, the GNC can be performed in the six subsystems to obtain the global stability feature. A detailed explanation will be given in Section 3.5.

It can be seen from Fig. 3(b) that a coupling relationship exists between the two subsystems of the established two-port circuit model of the LTC, since the controlled voltage source $\frac{Y_m v_R}{Y_s}$ and controlled current source $\frac{Y_m i_S}{Y_s}$ are determined by the voltage at the other terminal v_R and the current flowing through the other terminal i_S, respectively. In fact, the two subsystems can be regarded as decoupled from the perspective of impedance. In the IBSC, the controlled voltage and current sources slightly contribute to component impedance [18]. Thus, the controlled voltage and current sources can be neglected in the IBSC. In addition, Z_{short} and Y_{open} are not affected by the other subsystem, as shown in (8). This is why we use "impedance-decoupled network model" to represent the decoupling relationship, instead of simply using "decoupled network model".

3.5 Step 4: Stability Analysis Based on the Established DQ Impedance-Decoupled Network Model of the Whole OWPP

Based on Fig. 9(f), i_g can be calculated as

$$i_g = \frac{I_{N5} - V_g Y_{N5}}{1 + Z_g Y_{N5}} \quad (27)$$

Number of RHP poles of i_g can be calculated as [53]

$$P(i_g) = Z(1 + Z_g Y_{N5}) + P(I_{N5} - V_g Y_{N5})$$
$$= P(Y_{N5}) - N_{(-1,j0)}(Z_g Y_{N5}) + P(I_{N5}) \quad (28)$$

where $P(\bullet)$ and $Z(\bullet)$ indicate the numbers of RHP poles and zeros, respectively. $N_{(-1,j0)}(\bullet)$ indicates the encirclement number around $(-1, j0)$ in anticlockwise direction. In addition, numbers of RHP poles of I_{N1}-I_{N5} can be calculated based on (22)-(26), shown as

$$P(I_{N1}) = Z(1 + Z_{short1}Y_{GCI1}) + P(I_{GCI1})$$
$$= P(Y_{GCI1}) - N_{(-1,j0)}(Z_{short1}Y_{GCI1}) + P(I_{GCI1}) \quad (29)$$

$$P(I_{N2}) = Z(1 + Z_{short2}Y_{GCI2}) + P(I_{GCI2})$$
$$= P(Y_{GCI2}) - N_{(-1,j0)}(Z_{short2}Y_{GCI2}) + P(I_{GCI2}) \quad (30)$$

$$P(I_{N3}) = Z(1 + Z_{short3}(Y_{N1} + Y_{N2})) + P(I_{N1} + I_{N2})$$
$$= P(Y_{N1}) + P(Y_{N2}) - N_{(-1,j0)}(Z_{short3}(Y_{N1} + Y_{N2}))...$$
$$+P(I_{N1}) + P(I_{N2}) \quad (31)$$

$$P(I_{N4}) = Z(1 + Z_{short4}Y_{GCI3}) + P(I_{GCI3})$$
$$= P(Y_{GCI3}) - N_{(-1,j0)}(Z_{short4}Y_{GCI3}) + P(I_{GCI3}) \quad (32)$$

$$P(I_{N5}) = Z(1 + Z_{short5}(Y_{N3} + Y_{N4})) + P(I_{N3} + I_{N4})$$
$$= P(Y_{N3}) + P(Y_{N4}) - N_{(-1,j0)}(Z_{short5}(Y_{N3} + Y_{N4}))...$$
$$+P(I_{N3}) + P(I_{N4}) \quad (33)$$

Similarly, numbers of RHP poles of Y_{N1}-Y_{N5} can be calculated based on (22)-(26), shown as

$$P(Y_{N1}) = Z(1 + Z_{short1}Y_{GCI1}) + P(1 + Z_{open1}Y_{GCI1})$$
$$= P(Y_{GCI1}) - N_{(-1,j0)}(Z_{short1}Y_{GCI1}) \quad (34)$$

$$P(Y_{N2}) = Z(1 + Z_{short2}Y_{GCI2}) + P(1 + Z_{open2}Y_{GCI2})$$
$$= P(Y_{GCI2}) - N_{(-1,j0)}(Z_{short2}Y_{GCI2}) \quad (35)$$

$$P(Y_{N3}) = Z(1 + Z_{short3}(Y_{N1} + Y_{N2})) + P(1 + Z_{open3}$$
$$...(Y_{N1} + Y_{N2}))$$
$$= P(Y_{N1}) + P(Y_{N2}) - N_{(-1,j0)}(Z_{short3}$$
$$...(Y_{N1} + Y_{N2})) \quad (36)$$

$$P(i_g) = \underbrace{\sum_{i=1}^{3} P(Y_{GCIi})}_{=0} + \underbrace{\sum_{i=1}^{3} P(I_{GCIi})}_{=0} - \underbrace{N_{(-1,j0)}(Z_{short1}Y_{GCI1})}_{\text{Subsystem 1}} - \underbrace{N_{(-1,j0)}(Z_{short2}Y_{GCI2})}_{\text{Subsystem 2}} - \underbrace{N_{(-1,j0)}(Z_{short3}(Y_{N1}+Y_{N2}))}_{\text{Subsystem 3}}$$
$$\ldots - \underbrace{N_{(-1,j0)}(Z_{short4}Y_{GCI3})}_{\text{Subsystem 4}} - \underbrace{N_{(-1,j0)}(Z_{short5}(Y_{N3}+Y_{N4}))}_{\text{Subsystem 5}} - \underbrace{N_{(-1,j0)}(Z_g Y_{N5})}_{\text{Subsystem 6}} \quad (39)$$

$$\begin{aligned} P(Y_{N4}) &= Z(1+Z_{short4}Y_{GCI3}) + P(1+Z_{open4}Y_{GCI3}) \\ &= P(Y_{GCI3}) - N_{(-1,j0)}(Z_{short4}Y_{GCI3}) \end{aligned} \quad (37)$$

$$\begin{aligned} P(Y_{N5}) &= Z(1+Z_{short5}(Y_{N3}+Y_{N4})) + P(1+Z_{open5} \\ &\quad ...(Y_{N3}+Y_{N4})) \\ &= P(Y_{N3}) + P(Y_{N4}) - N_{(-1,j0)}(Z_{short5} \\ &\quad ...(Y_{N3}+Y_{N4})) \end{aligned} \quad (38)$$

(39) shown at the top of this page can be obtained by substituting (29)-(38) into (28). Since each GCI is stable in stand-alone mode, i.e., $P(Y_{GCIi}) = P(I_{GCIi}) = 0$ $(i = 1, 2, 3)$, the stability feature of i_g is determined by the rest six components in (39). It can be observed that the six encirclement numbers of (39) around $(-1, j0)$ in complex plane correspond to the six subsystems in Fig. 9, i.e., the stability of the whole OWPP in Fig. 7(a) can be obtained by assessing the stability of the six subsystems in Fig. 9. Specifically, if all the subsystems are stable, the complete system will be stable. Otherwise, the complete is probably unstable.

It can be seen from the derivation procedure that, similar conclusion can be obtained if there exists more GCIs and LTCs in the radial OWPP. In addition, although the derivation procedure is performed in phasor-domain for simplicity, it is also applicable in dq-domain. Note that the proposed dq impedance-decoupled network modelling method is independent on the control structures of the GCIs.

3.6 Some Issues Related with the Proposed Stability Analysis Method

3.6.1 Emphases of the Contributions: The impedance-decoupled modelling method of multi-port transmission network is initially presented in our previous works [13, 33]. This paper further improves the performances of the impedance-decoupled concept from the following three perspectives. First, the transmission line is merely regarded as an RL circuit model in [13, 33], whereas practical LTC model considering frequency-dependent characteristics of p.u.l. resistance and inductance is adopted in this paper. In addition, p.u.l. electrical parameters are extracted from measured one-end short-circuited and open-circuited impedances of a specific LTC. Second, the multi-port transmission topologies, e.g., three-port and four-port transmission topologies, are modelled as impedance-decoupled multi-port networks in [13, 33], whereas LTCs are modelled as impedance-decoupled two-port networks in this paper. Third, only inner current control loop of the GCI is modelled in [13, 33], which is only able to deal with high-frequency stability issue. On the other hand, both high-frequency and low-frequency stability issues are investigated in this paper by considering both inner current control loop and PLL simultaneously.

Next, the differences between this paper and [23] are summarized as follows. To avoid the RHP pole calculation of return-ratio matrices in the conventional impedance-based GNC, and enable stability assessment using only measured impedance frequency responses of system components without knowing internal information, the component connection method in the frequency-domain is proposed in [23] to derive the impedance matrix models of system connection network and aggregated inverter components. The system connection network as a whole and all inverter components as a whole are modelled as impedance matrix models, respectively. However, the proposed method in [23] suffers from the following two disadvantages. First, the derived impedance matrix models must be reconstructed, if connection network topology changes or new transmission lines/inverters are added/deleted. Second, the problematic inverter components cannot be identified, if the power system is assessed as unstable. To overcome aforementioned two disadvantages, impedance-decoupled two-port circuit model of the LTC is presented in this paper to decouple the whole system into several small subsystems. Due to the modular modelling method, the established impedance-decoupled system model can be easily reconstructed, if connection topology changes or components are added/deleted. In addition, the subsystems where GNC is not satisfied are identified as instability sources.

3.6.2 Stability Improvement under Weak Grid Conditions: This paper presents a dq impedance-decoupled modelling method of power electronic and LTC-dominated power systems to assess the stability characteristics with grid strength varying, instead of proposing stability improvement strategies under weak grid conditions. In fact, various stability improvement strategies have widely been explored, e.g., based on controller parameters retuning [52], based on active damping [38], based on passive damping [54], based on additional grid voltage feed-forward loop [55]. Details of these stability improvement strategies are not explained here.

3.6.3 Stability Analysis under Unbalanced Grid Conditions: Stability assessment under unbalanced grid conditions has been a hot topic recently [56–60]. Harmonic transfer functions are used in [56, 57] to derive the impedance model of unbalanced three-phase grid, which is able to capture all the possible frequency couplings. Based on the harmonic transfer-function-based model, it's found that the GCI-grid system exhibits a greater capability of maintaining stability if the grid asymmetry is more serve. Therefore, the presented stability analysis method in this paper for balanced systems provides a conservative stability conclusion, i.e., if the system is assessed as stable for a balanced system using the proposed method in this paper, the stability performance will be even better in the unbalanced system [56, 57].

In addition, an online frequency response measurement method of the grid dq impedance model under harmonics and unbalance is proposed in [58]. Furthermore, state-space models of GCIs and modular multilevel converters under unbalanced grid conditions are presented in [59] and [60], respectively, for small-signal stability analysis. To guarantee the stability of the GCIs under unbalanced grid conditions, a simple yet effective current-control-based compensator is also developed in [59]. Readers can find implementation details in these papers.

4 Implementation of the Proposed Stability Analysis Method

In this section, the proposed dq impedance-decoupled network model of Fig. 7(a) is first established based on the flowchart in Fig. 4. The proposed stability analysis method is then implemented.

Table 1 Circuit and Controller Parameters of Inverter of PMSG

Parameter	Value
DC-link voltage V_{dc}	1150 V
Grid voltage V_g (Phase-Phase Vrms)	575V
Grid fundamental frequency	50 Hz
Inverter side filter inductance L_{f1}	263 μH
Grid side filter inductance L_{f2}	200 μH
Filter capacitance C_f	100 μF
Filter inductance L_f for L filter	789 μH
Switching frequency f_{swit}	2.5 kHz
Sampling frequency f_{samp}	2.5 kHz
d axis current reference I_d^*	1.0 kA
q axis current reference I_q^*	0 A
Proportional gain of current controller k_{pi}	5.4908e-4
Integral gain of current controller k_{ii}	0.3295
Proportional gain of PLL k_{ppll}	20
Integral gain of PLL k_{ipll}	200

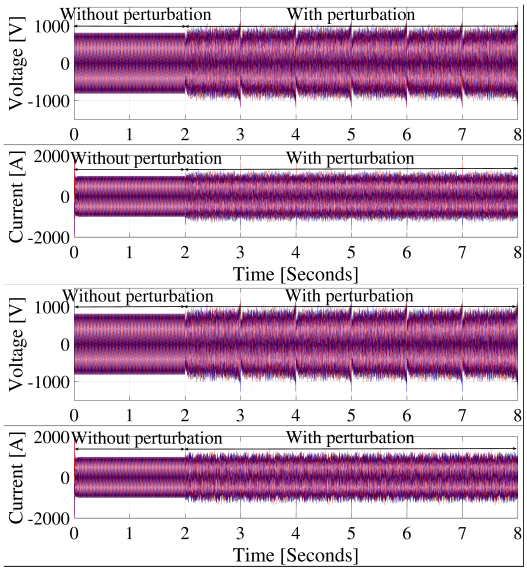

Fig. 10. Time-domain simulation waveforms of PCC voltage and grid current without voltage perturbation before 2 s and with voltage perturbation after 2 s. (a) The first perturbation. (b) The second perturbation.

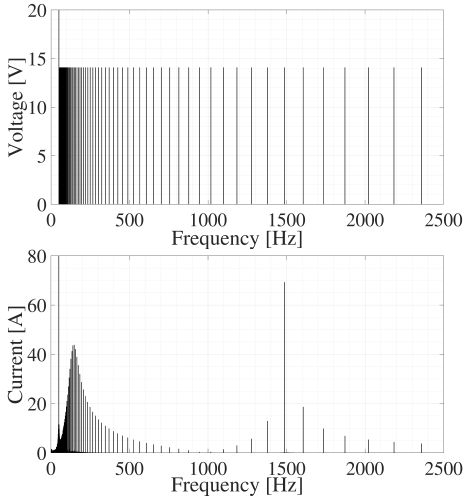

Fig. 11. FFT results of PCC voltage and grid current of the first perturbation. (a) FFT result of PCC voltage. (b) FFT result of grid current.

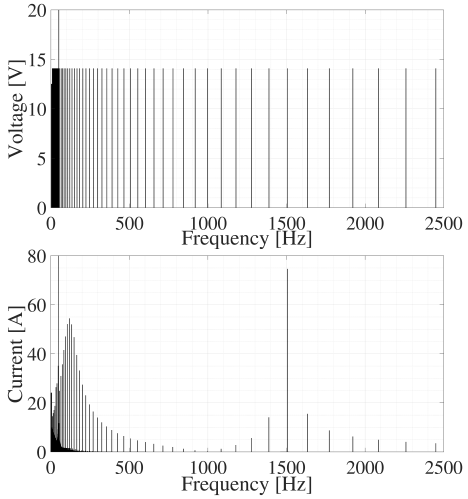

Fig. 12. FFT results of PCC voltage and grid current of the second perturbation. (a) FFT result of PCC voltage. (b) FFT result of grid current.

4.1 Step 1: Identification of DQ Impedance Models of GCIs Based on the MF Algorithm

Table 1 shows the circuit and controller parameters of the three GCIs in Fig. 7(a), where GCI 2 and GCI 3 are with LCL filter, and GCI 1 is with L filter. The ratio of filter resonance frequency ω_{res} and sampling frequency ω_{sam} plays an important role in the selection of active damping strategies [61]. If $\omega_{res} < \omega_{sam}/6$, an active damping strategy is mandatory for stable operation. If $\omega_{res} > \omega_{sam}/6$, an active damping strategy is not required for stable operation. If $\omega_{res} = \omega_{sam}/6$, the system will be unstable irrespective of the controller that is used. In this paper, $\omega_{res} = \sqrt{\frac{L_{f1}+L_{f2}}{L_{f1}L_{f2}C_f}} = 9382$ rad/s is higher than $\omega_{sam}/6 = 2618$ rad/s. Therefore, according to [61], the active damping strategy is not required for the stable operation of the GCIs in Table 1.

Two multi-tone small-signal voltage perturbations consisting of 80 frequency components which are logarithmically distributed between 1 Hz and 2.5 kHz are designed and injected into PCC in series way, as shown in Fig. 5. In addition, the magnitudes of the 80 frequency components are designed as 1% of PCC voltage magnitude, i.e. $\frac{\sqrt{6}V_g}{100} = 14.08$ V, which are not too large to influence the steady-state operating point of the GCI under study. Fig. 10 shows the two time-domain simulation waveforms of PCC voltage and grid current without perturbation before 2 s and with perturbation after 2 s. In addition, frequency spectrums of the two perturbed PCC voltages and grid currents after 2 s can then be obtained by performing FFT analysis, as shown in Figs. 11 and 12. The impedance frequency responses of the GCI at the 80 frequency points can then be calculated by dividing the two linear independent voltage components in Figs. 11(a) and 12(a) by the current response components in Figs. 11(b) and 12(b) at these frequency points, as shown in (12).

Bode plots of terminal impedance frequency responses of the LCL-filtered GCI derived by the theoretical dq impedance matrix formula in (2) and by frequency scanning method in Fig. 5 are shown as the red solid lines $\mathbf{Z_{dq\_LCL\_the}}$ and black crossed lines $\mathbf{Z_{dq\_LCL\_mea}}$ in Fig. 13, respectively. It can be seen that the measured and analytical terminal impedance frequency responses agree with each other well, which verifies the effectiveness of the frequency scanning method in Fig. 5 and correctness of the analytical dq impedance matrix in (2). The measured discrete terminal impedance frequency responses are fitted by both 6-order and 14-order transfer function matrices in form of (11) using the MF algorithm, shown as the blue solid and brown solid lines in Fig. 13, respectively. It can be seen that the fitting accuracy of the fitted 14-order transfer function matrix is higher than the fitted 6-order transfer function matrix. In addition, It can be seen from

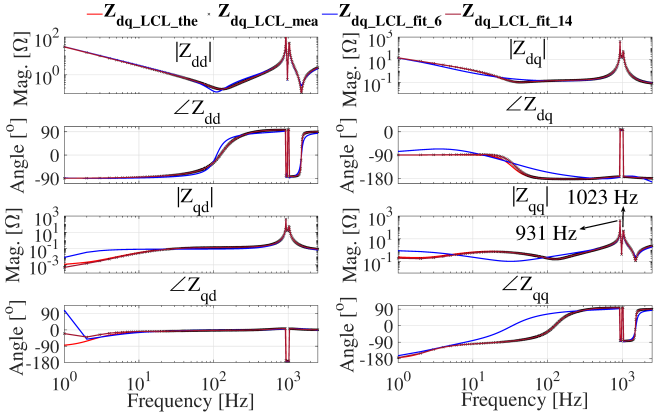

Fig. 13. Bode diagrams of theoretically-derived $\mathbf{Z_{dq\_LCL\_the}}$, frequency scanning-obtained $\mathbf{Z_{dq\_LCL\_mea}}$, fitted 6-order transfer function matrix $\mathbf{Z_{dq\_LCL\_fit\_6}}$ and fitted 14-order transfer function matrix $\mathbf{Z_{dq\_LCL\_fit\_14}}$ of LCL-filtered inverter of PMSG.

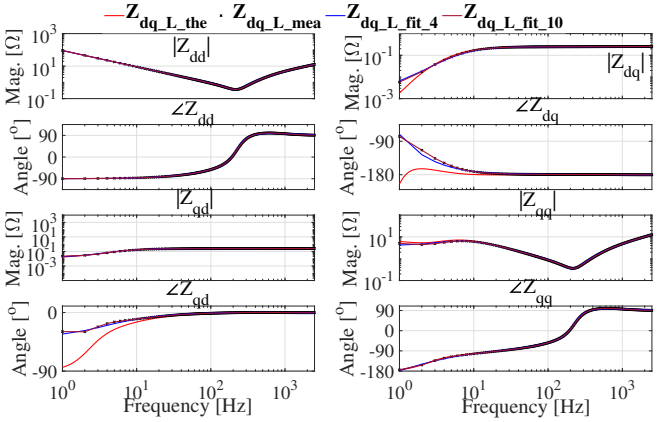

Fig. 14. Bode diagrams of theoretically-derived $\mathbf{Z_{dq\_L\_the}}$, frequency scanning-obtained $\mathbf{Z_{dq\_L\_mea}}$, fitted 4-order transfer function matrix $\mathbf{Z_{dq\_L\_fit\_4}}$ and fitted 10-order transfer function matrix $\mathbf{Z_{dq\_L\_fit\_10}}$ of L-filtered inverter of PMSG.

Table 2 Poles of the Fitted Transfer Function Matrices in Form of (11)

$\mathbf{Z_{dq\_LCL\_fit\_6}}$	$\mathbf{Z_{dq\_LCL\_fit\_14}}$	$\mathbf{Z_{dq\_L\_fit\_4}}$	$\mathbf{Z_{dq\_L\_fit\_10}}$
-0.23	0.06	-2514.00	-0.01
16.67	3.36	-44.54	-10.67
-0.57±i5.84e3	-10.21	-0.03	-36.76
1.80 ±i6.47e3	17.18	48.44	49.46
	-115.87		4.47±i5.40
	137.04		-5.00e3±i1.20e2
	-4307.00		-1.45e4±i2.01e5
	30064.00		
	-0.32±i5.84e3		
	1.24±i6.47e3		
	-6.61e3±i2.00e3		

Figs. 10 to 13 that, the MF algorithm is able to fit a smooth dq impedance curve from a small number of discrete impedance frequency responses, which could release the computational burdens of frequency scanning, if a large number of impedance frequency responses are desired.

The poles of the fitted 6-order and 14-order transfer function matrices are shown in the first and second columns of Table 2, respectively. The poles -0.57±i5.84e3 and -0.32±i5.84e3 are corresponding to frequency 929.46 Hz. In addition, 1.80±i6.47e3 and 1.24±i6.47e3 are corresponding to 1029.73 Hz. They agree with the two resonance peaks of magnitudes of Z_{dd} and Z_{qq}, i.e., 931 Hz and 1023 Hz, in Fig. 13. The ability of the fitted 6-order transfer function matrix to reproduce terminal impedance frequency responses in other frequency points is weaker than the fitted 14-order transfer function matrix, which indicates that the fitting ability can be improved by increasing fitting order.

In addition, the measured dq impedance frequency responses of the L-filtered inverter are also fitted by the MF algorithm. Bode plots of terminal impedance frequency responses of the L-filtered inverter derived by the theoretical dq impedance matrix formula in (1) and by frequency scanning method in Fig. 5 are shown as the red solid lines $\mathbf{Z_{dq\_L\_the}}$ and black crossed lines $\mathbf{Z_{dq\_L\_mea}}$ in Fig. 14, respectively. It can be seen that the measured and analytical terminal impedance frequency responses agree with each other well, which verifies the effectiveness of the frequency scanning method in Fig. 5 and correctness of the analytical dq impedance matrix in (1). The measured discrete terminal impedance frequency responses are fitted by both 4-order and 10-order transfer function matrices in form of (11) using the MF algorithm, shown as the blue solid and brown solid lines in Fig. 14, respectively. It can be seen that the fitting accuracy of the fitted 10-order transfer function matrix is higher than the fitted 4-order transfer function matrix. In addition, it can be seen from Figs. 13 and 14 that the order of the fitted transfer function matrix of the L-filtered inverter can be lower than that of the LCL-filtered inverter. Poles of the fitted 4-order and 10-order transfer function matrices are provided in the third and fourth columns of Table 2, respectively.

4.2 Step 2: P.u.l. Parameters Identification of LTC and DQ Impedance-Decoupled Two-Port Circuit Modelling

The line models provided by Simscape library of Matlab/Simulink, e.g., Distributed Parameters Line model and Pi Section Line, cannot reproduce the frequency-dependent characteristics of p.u.l. electrical parameters. To overcome this shortcoming of Simscape library, ARTEMiS-SSN library of OPAL-RT developed the advanced Modal/Marti and Phase/Wideband frequency-dependent line models, which can be directly used in Matlab/Simulink environment [62]. In this paper, the EMTP-RV program is used to calculate frequency-dependent p.u.l. resistance, inductance, and capacitance based on the line geometry and the conductor characteristics. The generated data is then saved and exported to the Wideband frequency-dependent line model. Next, the terminal impedance frequency responses of the Wideband frequency-dependent line model in dq-domain are measured in Matlab/Simulink environment based on the same frequency scanning scheme for GCIs.

Bode plots of the terminal impedance frequency responses of a 50 km LTC obtained by the frequency scanning method in Fig. 5 and the fitted results using the MF algorithm are shown as the red dotted line $\mathbf{Y_{short\_mea}}$ and black solid line $\mathbf{Y_{short\_fit}}$ in Fig. 15(a), respectively. It can be seen that the measured impedance frequency characteristics of the 50 km LTC can be well reproduced by the MF algorithm. On the basis of Fig. 15(a), the Bode plot of the one-end short-circuited phasor-domain admittance Y_{short} can be calculated based on (9), as shown in Fig. 15(b). In addition, the Bode plot of the one-end open-circuited phasor-domain admittance Y_{open} can also be calculated in a similar way.

The propagation constant γ can then be extracted from Y_{short} and Y_{open} using (13). It should be noted that inverse of hyperbolic function in (13) are multi-valued, since any $k \in Z$ satisfies the equation. The derived real part and imaginary part of γ by setting $k = 0$ are shown as the red solid line and blue solid line in Fig. 16, respectively. A pseudo code in Algorithm 1 is used to recover the actual imaginary part of γ, shown as the black solid line in Fig. 16. Finally, based on the calculated γ, Y_{short} and Y_{open}, p.u.l. parameters R', L', C' at each frequency point can be calculated using (14). The actual and extracted p.u.l. parameters using Algorithm 1 are plotted as blue solid lines and red dotted lines in Fig. 17, respectively. It can be seen that they highly agree with each other. In addition, the extracted p.u.l. parameters without correcting γ using Algorithm 1 are plotted as black lines in Fig. 17. It can be seen that the p.u.l.

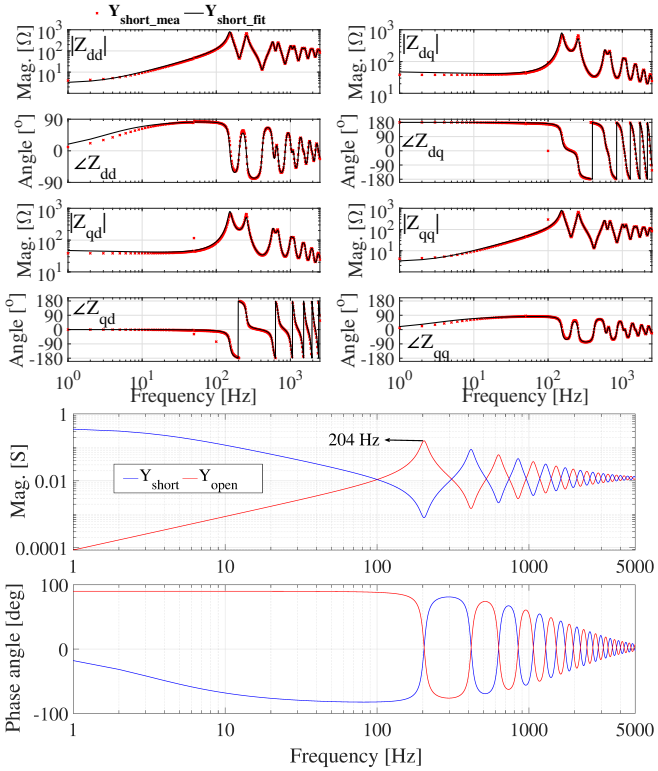

Fig. 15. Bode diagrams of terminal impedance frequency responses of a 50km LTC. (a) Measured one-end short-circuited admittance $\mathbf{Y_{short\_mea}}$ in dq-domain and fitted results $\mathbf{Y_{short\_fit}}$. (b) Derived Y_{short} and Y_{open} in phasor-domain based on (9).

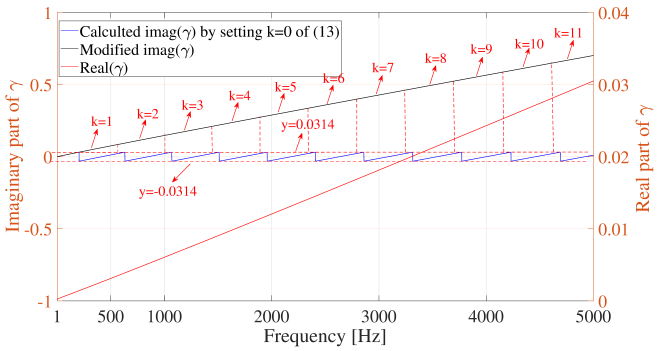

Fig. 16. Calculated propagation constant γ based on (13).

parameters can only be accurately extracted up to the first resonance frequency of Y_{open} in Fig. 15, i.e., 204 Hz. Based on the identified p.u.l. parameters, the two-port circuit models of LTCs can be established as Fig. 3(b).

4.3 Step 3: Establishment of the DQ Impedance-Decoupled Network Model of the Whole OWPP

Based on the fitted transfer function matrices of the dq impedance models of the GCIs and LTCs in Sections 4.1 and 4.2, six subsystems as shown in Fig. 9 can be established, where the parameters can be derived based on (22)-(26). The minor-loop gains of the six

Algorithm 1: Recover actual imaginary part of γ

```
set f_k as starting point, d_0 as LTC length and i = 0; while
  f_k is within frequency range of interest do
    update γ: imag(γ_{k_update}) = imag(γ_k) + iπ/d_0;
    if imag(γ_k) equals to π/(2d_0) then
      i = i + 1;
    end
end
```

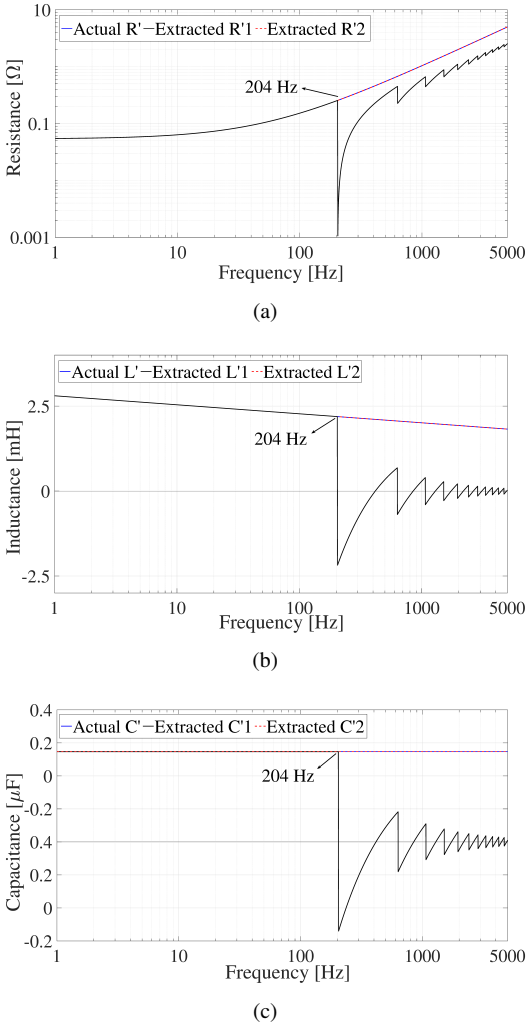

Fig. 17. Actual and extracted p.u.l. parameters. (a) P.u.l. resistance. (b) P.u.l. inductance. (c) P.u.l. capacitance.

subsystems in Fig. 9 can be calculated as

$$\begin{aligned}
\mathbf{T_{m1}} &= \mathbf{Z_{short1}}\mathbf{Y_{GCI1}} \\
\mathbf{T_{m2}} &= \mathbf{Z_{short2}}\mathbf{Y_{GCI2}} \\
\mathbf{T_{m3}} &= \mathbf{Z_{short3}}(\mathbf{Y_{N1}} + \mathbf{Y_{N2}}) \\
\mathbf{T_{m4}} &= \mathbf{Z_{short4}}\mathbf{Y_{GCI3}} \\
\mathbf{T_{m5}} &= \mathbf{Z_{short5}}(\mathbf{Y_{N3}} + \mathbf{Y_{N4}}) \\
\mathbf{T_{m6}} &= \mathbf{Z_g}\mathbf{Y_{N5}}
\end{aligned} \tag{40}$$

where the bold letters indicate that the impedance and admittance models are represented dq-domain. Based on (39), system stability can then be assessed by checking whether any Nyquist plots of the

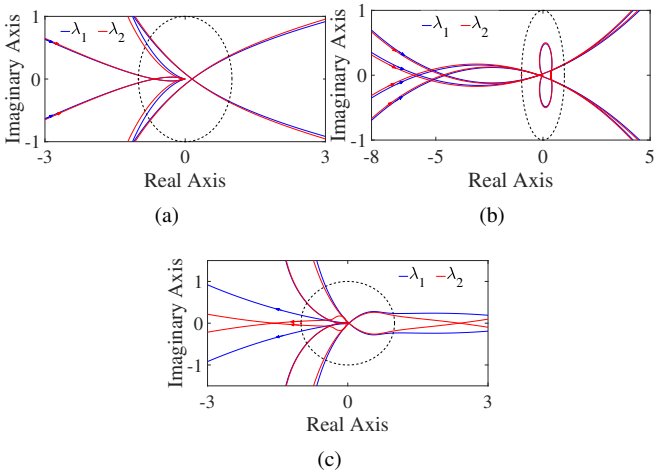

Fig. 18. Nyquist plots of the characteristic loci of the critical return ratio matrices in Fig. 9. (a) For subsystem 4 under case 1. (b) For subsystem 4 under case 2. (c) For subsystem 4 under case 3.

minor-loop gains in (40) encircle point $(-1, j0)$ in complex plane, as shown in Section 4.4.

4.4 Step 4: Stability Analysis Based on the DQ Impedance-Decoupled Network Model of the Whole OWPP

To simplify the verification of effectiveness of the established model in Fig. 9 for stability assessment of the radial OWPP in Fig. 7(a), Y_{sk} and Y_{mk} in Fig. 7(a) are regarded as constant, as shown in Fig. 6. In addition, resistances of the LTCs are also ignored, i.e., $Y_{sk} - Y_{mk} = \frac{sC_k}{2}$ and $Y_{mk} = \frac{1}{sL_k}$ $(k = 1, 2..., 5)$, where C_k and L_k are total capacitances and inductances of LTC k in Fig. 7(a), respectively. Therefore, the five dq-domain one-end short-circuited impedance models in (40), i.e. $\mathbf{Z_{short1}}$, $\mathbf{Z_{short2}}$,..., $\mathbf{Z_{short5}}$, can be modified as

$$\mathbf{Z_{shortk}} = \mathbf{Z_{L_k}} // \mathbf{Z_{C_k/2}} = \frac{\mathbf{Z_{L_k}} \mathbf{Z_{C_k/2}}}{\mathbf{Z_{Lk}} + \mathbf{Z_{C_k/2}}} \quad k \in [1, 5] \quad (41)$$

where $\mathbf{Z_{L_k}}$ and $\mathbf{Z_{C_k/2}}$ can be calculated using (42) and (44) in Appendix. The circuit and controller parameters of the three GCIs are shown in Table 1. In addition, the p.u.l. inductance and capacitance of the five LTCs are 0.1 mH/km and 3 μF/km, respectively. The effectiveness of the proposed stability analysis method will be verified by three cases, i.e., stable case, high-frequency unstable case and low-frequency unstable case.

In case 1, lengths of the five LTCs in Fig. 7(a) are $l_{LTC1} = 1$ km, $l_{LTC2} = 1$ km, $l_{LTC3} = 2$ km, $l_{LTC4} = 1$ km and $l_{LTC5} = 10$ km, respectively. The corresponding short-circuit ratio can be calculated as 3.43 [10]. Fig. 18(a) shows the Nyquist plots of the characteristic loci of the return ratio matrix in Subsystem 4 of Fig. 9 (In cases 1-3, only the Nyquist plots of problematic submodules are plotted.). It can be seen that no Nyquist plots of characteristic loci encircles $(-1, j0)$, which indicates that i_g is stable according to (39).

In case 2, l_{LTC4} is increased from 1 km to 10 km, i.e., the short-circuit ratio is decreased from 3.43 to 2.14. Fig. 18(b) shows the Nyquist plots of the characteristic loci of the return ratio matrix in Subsystem 4 of Fig. 9. It can be seen that both λ_1 and λ_2 encircle $(-1, j0)$ two times, which indicates that i_g is unstable at two frequency points according to (39).

In case 3, l_{LTC4} is further increased from 10 km to 130 km, i.e., the short-circuit ratio is further decreased from 2.14 to 0.36. Fig. 18(c) shows the Nyquist plots of the characteristic loci of the return ratio matrix in Subsystem 4 of Fig. 9. It can be seen that λ_2 encircles $(-1, j0)$ one time, which indicates that i_g is unstable according to (39).

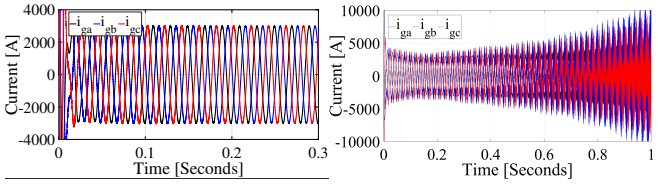

Fig. 19. Time-domain simulation results of grid currents i_g under cases 1 and 2 based on Matlab/Simulink platform. (a) Case 1. (b) Case 2.

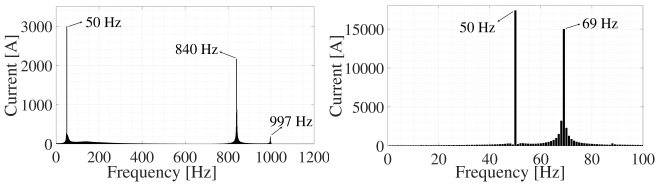

Fig. 20. Frequency spectrum of i_g under cases 2 and 3 based on Matlab/Simulink platform. (a) Case 2. (b) Case 3.

5 Simulation and Real-Time Verifications

In this section, the correctness of the stability analysis results in Section 4.4 is verified by time-domain simulation results based on Matlab/Simulink platform and real-time verification based on OPAL-RT platform.

5.1 Simulation Verification Based on Matlab/Simulink Platform

Fig. 19 shows the time-domain simulation results of grid current i_g under cases 1 and 2. It can be seen that i_g is stable under case 1, and high-frequency instability phenomena occur under case 2. The frequency spectrum of i_g under case 2 is shown in Fig. 20(a), where electrical oscillation occurs at 840 Hz and 997 Hz. The time-domain simulation results in Figs. 19 and 20(a) agree with the stability analysis results in Figs. 18(a) and 18(b).

In addition, Fig. 21 shows the time-domain simulation results of grid current i_g and output currents of the three GCIs under case 3. It can be seen that the grid current i_g and the output current the GCI 3 i_3 are unstable, whereas the output currents of GCIs 1 and 2, i.e., i_1 and i_2, are stable. Fig. 20(b) shows the frequency spectrum of i_g, where low-frequency electrical oscillation occurs at 69 Hz. It can be concluded that the instability phenomena result from GCI 3. On the other hand, Fig. 18(c) shows that the instability phenomena result from the subsystem 4 in Fig. 9. The time-domain simulation results in Figs. 21 and 20(b), thus, verify the correctness of the stability analysis results in Fig. 18(c).

5.2 Real-Time Verification Based on OPAL-RT Platform

Real-time verification based on OPAL-RT digital simulator platform is performed to further validate the correctness of the theoretical analysis results in Section 4.4 and the time-domain simulation results obtained by Matlab/Simulink platform in Section 5.1. The picture of the OPAL-RT platform in laboratory is shown in Fig. 22, which consists of an OP5600 real-time digital simulator and a monitor. Backed by nearly two decades of expertise in the development of

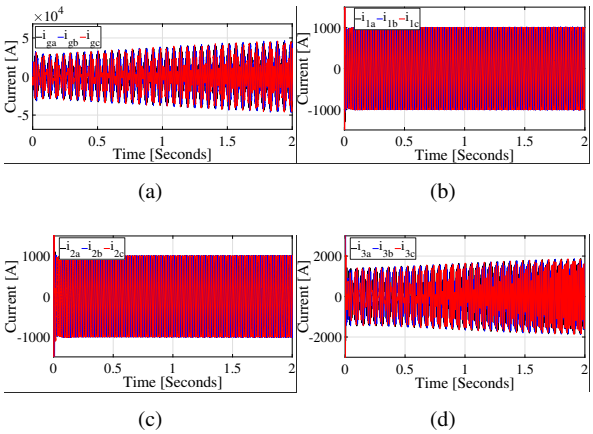

Fig. 21. Time-domain simulation results of grid currents i_g and GCI output currents under case 3 based on Matlab/Simulink platform. (a) Grid current i_g. (b) Output current of GCI 1 i_1. (c) Output current of GCI 2 i_2. (d) Output current of GCI 3 i_3.

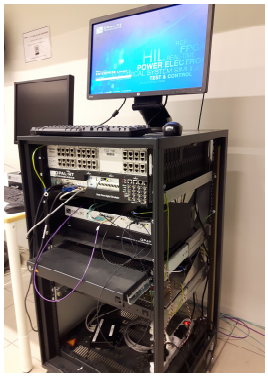

Fig. 22. Picture of the OPAL-RT platform in laboratory.

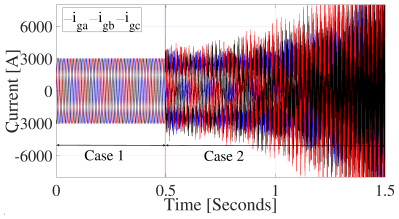

Fig. 23. Real-time verification of grid currents i_g when the system changes from case 1 to case 2 at 0.5 s based on OPAL-RT platform.

high-performance simulation hardware, the OP5600 real-time simulator is the most adopted simulation platform by OPAL-RT's users in both industry and academia. OP5600 combines the performance, versatility and reliability that is ideal for demanding hardware-in-the-loop applications. The Simulink-based model is first established in the RT-LAB software, based on which code is generated and downloaded into the OP5600 hardware. The real-time simulation results obtained by OPAL-RT platform are then post-processed in Matlab software.

Fig. 23 shows the simulation results of grid current i_g when the system changes from case 1 to case 2 at 0.5 s. It can be seen i_g is stable before 0.5 s, and unstable after 0.5 s. The frequency spectrum of i_g after 0.5 s is shown in Fig. 24(a), where i_g oscillates at 840 Hz and 997 Hz. The real-time verification results in Figs. 23 and 24(a) agree with the time-domain simulation results in Figs. 19 and 20(a).

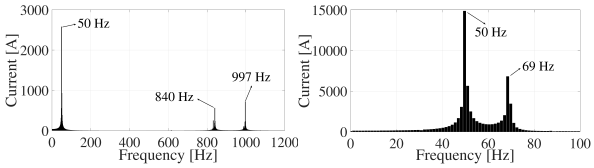

Fig. 24. Frequency spectrum of i_g under cases 2 and 3 based on OPAL-RT platform. (a) Case 2. (b) Case 3.

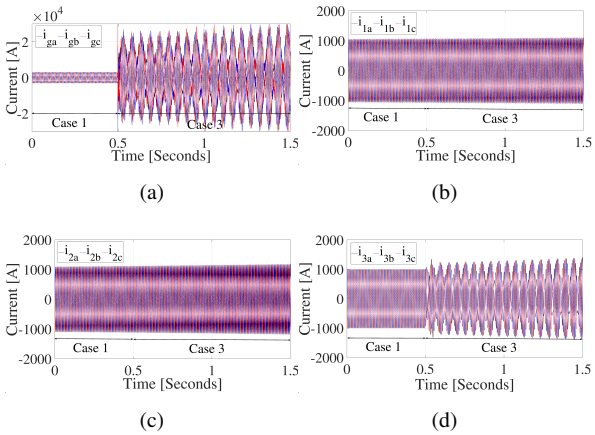

Fig. 25. Time-domain simulation results of grid currents i_g and GCI output currents under case 3 based on OPAL-RT platform. (a) Grid current i_g. (b) Output current of GCI 1 i_1. (c) Output current of GCI 2 i_2. (d) output current of GCI 3 i_3.

Furthermore, Fig. 25 shows the simulation results of grid current i_g and output currents of the three GCIs when the system changes from case 1 to case 3 at 0.5 s. It can be seen that, all the four currents are stable before 0.5 s, whereas i_g and i_3 are unstable, i_1 and i_2 are stable after 0.5 s. The frequency spectrum of i_g after 0.5 s is shown in Fig. 24(b), where i_g oscillates at 69 Hz. The real-time verification results in Figs. 25 and 24(b) agree with the time-domain simulation results in Figs. 21 and 20(b).

6 Conclusion

This paper presents a frequency scanning-based dq impedance-decoupled network model of OWPPs for stability analysis. The dq impedance models of GCIs are fitted from measured terminal impedance frequency responses using the MF algorithm. In addition, p.u.l electrical parameters of the LTCs are extracted from measured terminal impedance frequency responses of a specific LTC, based on which the dq impedance models of the LTCs in other lengths are theoretically calculated. The impedance-decoupled two-port network model of LTCs are then established to partition the whole OWPP into several subsystems. Furthermore, an impedance aggregation method for adjacent GCI and LTC based on one-end open-circuited admittance of the LTC is presented to decouple the subsystems. In addition, the p.u.l. electrical parameters of the LTCs can be extracted accurately based on the presented method. Instability phenomena and corresponding instability source of the OWPP in both low-frequency and high-frequency ranges are able to be predicted by the proposed dq impedance-decoupled network model. Both the time-domain simulation results based on Matlab/Simulink platform and real-time verification results based on OPAL-RT platform validate the effectiveness of the proposed stability analysis method. Compared with conventional IBSCs, RHP poles calculation can be

avoided. In addition, the instability source can be identified once GNC is not satisfied in any subsystems. In our near future work, circuit and controller parameters of the GCIs will be identified from the measured dq impedance frequency responses, which enables the further identification of problematic circuit and controller parameters contributing to the instability phenomena.

7 Acknowledgments

This work was supported by the ForskEL and EUDP project "Voltage Control and Protection for a Grid towards 100% Power Electronics and Cable Network (COPE)" (Project No.: 880063).

8 Appendix: Detailed Representation of Symbols in DQ Impedance Matrices (1) and (2)

$$\mathbf{Z}_{L_{f1}} = \begin{bmatrix} sL_{f1} & -\omega_1 L_{f1} \\ \omega_1 L_{f1} & sL_{f1} \end{bmatrix} \tag{42}$$

$$\mathbf{Z}_{L_{f2}} = \begin{bmatrix} sL_{f2} & -\omega_1 L_{f2} \\ \omega_1 L_{f2} & sL_{f2} \end{bmatrix} \tag{43}$$

$$\mathbf{Z}_{C_f} = \begin{bmatrix} \frac{s}{(s^2+\omega_1^2)C_f} & \frac{\omega_1}{(s^2+\omega_1^2)C_f} \\ -\frac{\omega_1}{(s^2+\omega_1^2)C_f} & \frac{s}{(s^2+\omega_1^2)C_f} \end{bmatrix} \tag{44}$$

For LCL-filtered VSC,

$$\begin{aligned} \mathbf{Y^c_{LCL}} &= ((\mathbf{Z^{-1}_{L_{f1}}}+\mathbf{Z^{-1}_{C_f}})^{-1}+\mathbf{Z_{L_{f2}}})^{-1} \\ \mathbf{Y^g_{LCL}} &= (\mathbf{Z}_{L2}(\mathbf{I}+(\mathbf{Z^{-1}_{L_{f2}}}+\mathbf{Z^{-1}_{C_f}})\mathbf{Z_{L_{f1}}}))^{-1} \end{aligned} \tag{45}$$

For L-filtered VSC,

$$\mathbf{Y^c_L} = \mathbf{Y^g_L} = \mathbf{Z^{-1}_{L_{f1}}} \tag{46}$$

$$\mathbf{G_{del}} = \begin{bmatrix} e^{-1.5T_s s} & 0 \\ 0 & e^{-1.5T_s s} \end{bmatrix} \tag{47}$$

where T_s is the sampling period.

$$\mathbf{G_{ci}} = \begin{bmatrix} k_{pi} + \frac{k_{ii}}{s} & 0 \\ 0 & k_{pi} + \frac{k_{ii}}{s} \end{bmatrix} \tag{48}$$

where k_{pi} and k_{ii} are proportional and integrator coefficients of current controller, respectively. V_{dc} is taken into account to design k_{pi} and k_{ii}.

$\mathbf{G^i_{PLL}}$ models the small-signal perturbation path from the system voltage to current in the controller dq frame.

$$\mathbf{G^i_{PLL}} = \begin{bmatrix} 0 & I^s_q G_{PLL} \\ 0 & -I^s_d G_{PLL} \end{bmatrix} \tag{49}$$

where I^s_d and I^s_q are d-axis and q-axis components of three-phase currents in system reference frame. G_{PLL} is defined as

$$G_{PLL} = \frac{k_{ppll} + k_{ipll}/s}{s + V^s_d(k_{ppll} + k_{ipll}/s)} \tag{50}$$

where k_{ppll} and k_{ipll} are proportional and integrator coefficients of PLL, respectively; V^s_d the d-axis component of three-phase terminal voltages in system reference frame.

$\mathbf{G^d_{PLL}}$ models the small-signal perturbation path from the system voltage to duty cycle in the controller dq frame.

$$\mathbf{G^d_{PLL}} = \begin{bmatrix} 0 & -D^s_q G_{PLL} \\ 0 & D^s_d G_{PLL} \end{bmatrix} \tag{51}$$

where D^s_d and D^s_q are d-axis and q-axis components of three-phase duty cycles in system reference frame.

9 References

[1] Liserre, M., Cardenas, R., Molinas, M., Rodriguez, J.: 'Overview of multi-MW wind turbines and wind parks', *IEEE Trans. Ind. Electron.*, 2011, **58**, (4), pp. 1081–1095

[2] Blaabjerg, F., Chen, Z., Kjaer, S.B.: 'Power electronics as efficient interface in dispersed power generation systems', *IEEE Trans. Power Electron.*, 2004, **19**, (5), pp. 1184–1194

[3] Zhang, S., Jiang, S., Lu, X., Ge, B., Peng, F.Z.: 'Resonance issues and damping techniques for grid-connected inverters with long transmission cable', *IEEE Trans. Power Electron.*, 2014, **29**, (1), pp. 110–120

[4] Ebrahimzadeh, E., Blaabjerg, F., Wang, X., Bak, C.L.: 'Harmonic stability and resonance analysis in large PMSG-based wind power plants', *IEEE Trans. Sustain. Energy*, 2018, **9**, (1), pp. 12–23

[5] Zhang, X., Chung, H.S.h., Cao, L.L., Chow, J.P.W., Wu, W. 'Impedance-based stability criterion for multiple offshore inverters connected in parallel with long cables'. In: Proc. 2017 IEEE Energy Conversion Congress and Exposition (ECCE). pp. 3383–3389

[6] Ruddy, J., Meere, R., O'Loughlin, C., O'Donnell, T.: 'Design of VSC connected low frequency AC offshore transmission with long HVAC cables', *IEEE Trans. Power Del.*, 2018, **33**, (2), pp. 960–970

[7] Zhou, J.Z., Ding, H., Fan, S., Zhang, Y., Gole, A.M.: 'Impact of short-circuit ratio and phase-locked-loop parameters on the small-signal behavior of a VSC-HVDC converter', *IEEE Trans. Power Del.*, 2014, **29**, (5), pp. 2287–2296

[8] Wen, B., Boroyevich, D., Burgos, R., Mattavelli, P., Shen, Z.: 'Analysis of DQ small-signal impedance of grid-tied inverters', *IEEE Trans. Power Electron.*, 2016, **31**, (1), pp. 675–687

[9] Lu, D., Wang, X., Blaabjerg, F.: 'Impedance-based analysis of DC-link voltage dynamics in voltage-source converters', *IEEE Trans. Power Electron.*, 2019, **34**, (4), pp. 3973–3985

[10] Zhou, W., Wang, Y., Torres.Olguin, R.E., Chen, Z.: 'Effect of reactive power characteristic of offshore wind power plant on low-frequency stability', *IEEE Trans. Energy Convers.*, Early Access, doi:10.1109/TEC.2020.2965017,

[11] Zhou, W., Wang, Y., Liu, D., Chen, Z. 'Optimization of active and reactive power dispatch among multi-paralleled grid-connected inverters considering low-frequency stability'. In: Proc. IEEE 45th Annual Conference of the IEEE Industrial Electronics Society (IES). pp. 6024–6031

[12] Wang, X., Blaabjerg, F.: 'Harmonic stability in power electronic-based power systems: Concept, modeling, and analysis', *IEEE Trans. Smart Grid*, 2019, **10**, (3), pp. 2858–2870

[13] Zhou, W., Wang, Y., Chen, Z.: 'Impedance-decoupled modelling method of multi-port transmission network in inverter-fed power plant', *IEEE Trans. Ind. Appl.*, 2020, **56**, (1), pp. 611–621

[14] Zhou, W., Torres.Olguin, R.E., Wang, Y., Chen, Z.: 'A gray-box hierarchical oscillatory instability source identification method of multiple-inverter-fed power systems', *IEEE J. Emerg. Sel. Topics Power Electron.*, Early Access, doi:10.1109/JESTPE.2020.2992225,

[15] Beerten, J., D'Arco, S., Suul, J.A.: 'Identification and small-signal analysis of interaction modes in VSC MTDC systems', *IEEE Trans. Power Del.*, 2016, **31**, (2), pp. 888–897

[16] Guo, C., Liu, W., Zhao, C., Iravani, R.: 'A frequency-based synchronization approach for the VSC-HVDC station connected to a weak AC grid', *IEEE Trans. Power Del.*, 2017, **32**, (3), pp. 1460–1470

[17] Li, T., Gole, A.M., Zhao, C.: 'Harmonic instability in MMC-HVDC converters resulting from internal dynamics', *IEEE Trans. Power Del.*, 2016, **31**, (4), pp. 1738–1747

[18] Sun, J.: 'Impedance-based stability criterion for grid-connected inverters', *IEEE Trans. Power Electron.*, 2011, **26**, (11), pp. 3075–3078

[19] Segundo.Ramirez, J., Bayo.Salas, A., Esparza, M., Beerten, J., Gómez, P.: 'Frequency domain methods for accuracy assessment of wideband models in electromagnetic transient stability studies', *IEEE Trans. Power Del.*, 2020, **35**, (1), pp. 71–83

[20] Wen, B., Boroyevich, D., Burgos, R., Mattavelli, P., Shen, Z.: 'Analysis of DQ small-signal impedance of grid-tied inverters', *IEEE Trans. Power Electron.*, 2016, **31**, (1), pp. 675–687

[21] Jamshidifar, A., Jovcic, D.: 'Small-signal dynamic DQ model of modular multilevel converter for system studies', *IEEE Trans. Power Del.*, 2016, **31**, (1), pp. 191–199

[22] Shuai, Z., Li, Y., Wu, W., Tu, C., Luo, A., Shen, Z.J.: 'Divided DQ small-signal model: A new perspective for the stability analysis of three-phase grid-tied inverters', *IEEE Trans. Ind. Electron.*, 2019, **66**, (8), pp. 6493–6504

[23] Cao, W., Ma, Y., Yang, L., Wang, F., Tolbert, L.M.: 'D–Q impedance based stability analysis and parameter design of three-phase inverter-based AC power systems', *IEEE Trans. Ind. Electron.*, 2017, **64**, (7), pp. 6017–6028

[24] Liu, H., Xie, X., Gao, X., Liu, H., Li, Y.: 'Stability analysis of SSR in multiple wind farms connected to series-compensated systems using impedance network model', *IEEE Trans. Power Syst.*, 2018, **33**, (3), pp. 3118–3128

[25] Liu, H., Xie, X., Liu, W.: 'An oscillatory stability criterion based on the unified dq-frame impedance network model for power systems with high-penetration renewables', *IEEE Trans. Power Syst.*, 2018, **33**, (3), pp. 3472–3485

[26] Zhang, C., Molinas, M., Rygg, A., Cai, X.: 'Impedance-based analysis of interconnected power electronics systems: Impedance network modeling and comparative studies of stability criteria', *IEEE J. Emerg. Sel. Topics Power Electron.*, Early Access, doi:10.1109/JESTPE.2019.2914560,

[27] Rygg, A., Molinas, M.: 'Apparent impedance analysis: A small-signal method for stability analysis of power electronic-based systems', *IEEE J. Emerg. Sel. Topics Power Electron.*, 2017, **5**, (4), pp. 1474–1486

[28] Bakhshizadeh, M.K., Blaabjerg, F., Hjerrild, J., Kocewiak, Ł., Bak, C.L.: 'Improving the impedance-based stability criterion by using the vector fitting

method', *IEEE Trans. Energy Convers.*, 2018, **33**, (4), pp. 1739–1747
[29] Bakhshizadeh, M.K., Yoon, C., Hjerrild, J., Bak, C.L., Kocewiak, Ł.H., Blaabjerg, F., et al.: 'The application of vector fitting to eigenvalue-based harmonic stability analysis', *IEEE J. Emerg. Sel. Topics Power Electron.*, 2017, **5**, (4), pp. 1487–1498
[30] Hong, L., Shu, W., Wang, J., Mian, R.: 'Harmonic resonance investigation of a multi-inverter grid-connected system using resonance modal analysis', *IEEE Trans. Power Del.*, 2019, **34**, (1), pp. 63–72
[31] Zhan, Y., Xie, X., Liu, H., Liu, H., Li, Y.: 'Frequency-domain modal analysis of the oscillatory stability of power systems with high-penetration renewables', *IEEE Trans. Sustain. Energy*, 2019, **10**, (3), pp. 1534–1543
[32] Yoon, C., Bai, H., Wang, X., Bak, C.L., Blaabjerg, F. 'Regional modeling approach for analyzing harmonic stability in radial power electronics based power system'. In: Proc. 2015 IEEE Power Electronics for Distributed Generation Systems (PEDG). pp. 1–5
[33] Zhou, W., Wang, Y., Chen, Z. 'Decoupled multi-port impedance modelling method of transmission network in inverter-fed power plant'. In: Proc. 2018 IEEE International Conference on Smart Grid (icSmartGrid). pp. 129–135
[34] Cao, W., Zhang, X., Ma, Y., Wang, F. 'Stability criterion and controller parameter design of radial-line renewable systems with multiple inverters'. In: Proc. 2016 IEEE Applied Power Electronics Conference and Exposition (APEC). pp. 2229–2236
[35] Gustavsen, B., Semlyen, A.: 'Rational approximation of frequency domain responses by vector fitting', *IEEE Trans. Power Del.*, 1999, **14**, (3), pp. 1052–1061
[36] Zhou, W., Wang, Y., Chen, Z. 'Impedance-based modelling method for length-scalable long transmission cable for stability analysis of grid-connected inverter'. In: Proc. 2018 IEEE 4th Southern Power Electronics Conference (SPEC). pp. 1–8
[37] Song, Y., Ebrahimzadeh, E., Blaabjerg, F.: 'Analysis of high-frequency resonance in DFIG-based offshore wind farm via long transmission cable', *IEEE Trans. Energy Convers.*, 2018, **33**, (3), pp. 1036–1046
[38] Chen, H.C., Cheng, P.T., Wang, X.: 'A passivity-based stability analysis of the active damping technique in the offshore wind farm applications', *IEEE Trans. Ind. Appl.*, 2018, **54**, (5), pp. 5074–5082
[39] Zhou, W., Wang, Y., Chen, Z. 'Frequency and temperature-dependent power cable modelling for small-signal stability analysis of grid-connected inverter system'. In: Proc. 2018 IEEE 4th Southern Power Electronics Conference (SPEC). pp. 1–8
[40] Beerten, J., D'Arco, S., Suul, J.A.: 'Frequency-dependent cable modelling for small-signal stability analysis of VSC-HVDC systems', *IET Gener. Transm. Distrib.*, 2016, **10**, (6), pp. 1370–1381
[41] Zhou, W., Wang, Y., Chen, Z. 'Vector fitting-based reduced order modelling method for power cables'. In: Proc. IET 15th International Conference on AC and DC Power Transmission (ACDC 2019). pp. 1–6
[42] Stevanovic, I., Wunsch, B., Madonna, G.L., Skibin, S.: 'High-frequency behavioral multiconductor cable modeling for EMI simulations in power electronics', *IEEE Trans. Ind. Informat.*, 2014, **10**, (2), pp. 1392–1400
[43] Wunsch, B., Stevanović, I., Skibin, S.: 'Length-scalable multiconductor cable modeling for EMI simulations in power electronics', *IEEE Trans. Power Electron.*, 2017, **32**, (3), pp. 1908–1916
[44] Harnefors, L., Bongiorno, M., Lundberg, S.: 'Input-admittance calculation and shaping for controlled voltage-source converters', *IEEE Trans. Ind. Electron.*, 2007, **54**, (6), pp. 3323–3334
[45] Harnefors, L., Wang, X., Yepes, A.G., Blaabjerg, F.: 'Passivity-based stability assessment of grid-connected VSCs—an overview', *IEEE J. Emerg. Sel. Topics Power Electron.*, 2016, **4**, (1), pp. 116–125
[46] Ebrahimzadeh, E., Blaabjerg, F., Wang, X., Bak, C.L.: 'Reducing harmonic instability and resonance problems in PMSG-based wind farms', *IEEE J. Emerg. Sel. Topics Power Electron.*, 2018, **6**, (1), pp. 73–83
[47] Cheah.Mane, M., Sainz, L., Liang, J., Jenkins, N., Ugalde.Loo, C.E.: 'Criterion for the electrical resonance stability of offshore wind power plants connected through HVDC links', *IEEE Trans. Power Syst.*, 2017, **32**, (6), pp. 4579–4589
[48] Rygg, A., Molinas, M., Zhang, C., Cai, X.: 'On the equivalence and impact on stability of impedance modeling of power electronic converters in different domains', *IEEE J. Emerg. Sel. Topics Power Electron.*, 2017, **5**, (4), pp. 1444–1454
[49] Zhang, C., Cai, X., Molinas, M., Rygg, A.: 'On the impedance modeling and equivalence of AC/DC-side stability analysis of a grid-tied type-IV wind turbine system', *IEEE Trans. Energy Convers.*, 2019, **34**, (2), pp. 1000–1009
[50] Xu, Y., Nian, H., Chen, L.: 'Small-signal modeling and analysis of DC-link dynamics in type-IV wind turbine system', *IEEE Trans. Ind. Electron.*, Early Access, doi:10.1109/TIE.2020.2970690,
[51] Paul, C.R.: 'Analysis of multiconductor transmission lines'. (John Wiley & Sons, USA, 2008)
[52] Amin, M., Molinas, M.: 'A gray-box method for stability and controller parameter estimation in HVDC-connected wind farms based on nonparametric impedance', *IEEE Trans. Ind. Electron.*, 2019, **66**, (3), pp. 1872–1882
[53] Liu, F., Liu, J., Zhang, H., Xue, D.: 'Stability issues of Z+ Z type cascade system in hybrid energy storage system (HESS)', *IEEE Trans. Power Electron.*, 2014, **29**, (11), pp. 5846–5859
[54] Wu, W., Sun, Y., Huang, M., Wang, X., Wang, H., Blaabjerg, F., et al.: 'A robust passive damping method for LLCL-filter-based grid-tied inverters to minimize the effect of grid harmonic voltages', *IEEE Trans. Power Electron.*, 2014, **29**, (7), pp. 3279–3289
[55] Zhang, X., Xia, D., Fu, Z., Wang, G., Xu, D.: 'An improved feedforward control method considering PLL dynamics to improve weak grid stability of grid-connected inverters', *IEEE Trans. Ind. Appl.*, 2018, **54**, (5), pp. 5143–5151
[56] Bakhshizadeh, M.K., Blaabjerg, F., Hjerrild, J., Wang, X., Kocewiak, Ł., Bak, C.L.: 'A numerical matrix-based method for stability and power quality studies based on harmonic transfer functions', *IEEE J. Emerg. Sel. Topics Power Electron.*, 2017, **5**, (4), pp. 1542–1552
[57] Zhang, C., Molinas, M., Rygg, A., Lyu, J., Cai, X.: 'Harmonic transfer-function-based impedance modeling of a three-phase VSC for asymmetric AC grid stability analysis', *IEEE Trans. Power Electron.*, 2019, **34**, (12), pp. 12552–12566
[58] Luhtala, R., Alenius, H., Messo, T., Roinila, T.: 'Online frequency-response measurements of grid-connected systems in presence of grid harmonics and unbalance', *IEEE Trans. Power Electron.*, 2020, **35**, (4), pp. 3343–3347
[59] Mortazavian, S., Shabestary, M.M., Mohamed, Y.A.R.I.: 'Analysis and dynamic performance improvement of grid-connected voltage–source converters under unbalanced network conditions', *IEEE Trans. Power Electron.*, 2017, **32**, (10), pp. 8134–8149
[60] Guo, C., Yang, J., Zhao, C.: 'Investigation of small-signal dynamics of modular multilevel converter under unbalanced grid conditions', *IEEE Trans. Ind. Electron.*, 2019, **66**, (3), pp. 2269–2279
[61] Parker, S.G., McGrath, B.P., Holmes, D.G.: 'Regions of active damping control for LCL filters', *IEEE Trans. Ind. Appl.*, 2014, **50**, (1), pp. 424–432
[62] ARTEMiS SSN.library. accessed: 2020-03-1. `https://www.opal-rt.com/solver-artemis-ssn/`